Stony Brook University

The Construction and Commissioning of a Hadron Blind Detector for PHENIX at RHIC

A Thesis Presented

by

William Anderson

to

The Graduate School

in Partial fulfillment of the

Requirements

for the Degree of

Master of Science

in

Physics
(Scientific Instrumentation)

Stony Brook University

August 2007

Stony Brook University

The Graduate School

William Anderson

We, the thesis committee for the above candidate for the

Master of Science degree,

hereby recommend acceptance of this thesis.

Prof. Thomas Hemmick
Thesis Advisor
Dept. of Physics and Astronomy

Peter Stephens
Chairperson of Defense Committee
Dept. of Physics and Astronomy

John Hobbs
Committee Member
Dept. of Physics and Astronomy

Peter Koch
Committee Member
Dept. of Physics and Astronomy

This thesis is accepted by the Graduate School

Lawrence Martin
Dean of the Graduate School

Abstract of the Thesis

The Construction and Commissioning of a Hadron Blind Detector for PHENIX at the RHIC

by

William Anderson

Master of Science

in

Physics
(Scientific Instrumentation)

Stony Brook University

2007

Abstract **- A Hadron Blind Detector (HBD) has been constructed as part of the detector upgrade program for the PHENIX experiment at RHIC. The HBD is a proximity focused windowless Cherenkov detector operated with pure CF_4 that will be used to detect single and double electrons in relativistic heavy ion collisions and provide additional rejection power against Dalitz pairs and photon conversions. The detector consists of a 50 cm long radiator directly coupled to a set of triple GEM detectors equipped with *CsI* photocathodes to detect UV photons produced by electrons emitting Cherenkov light. After a lengthy prototype development process, the final detector has now been constructed and installed in PHENIX where it took part in RHIC Run 07. The techniques used to develop and produce the photocathodes, as well as on the vessel assembly and initial testing of the final detector, are presented in this paper.**

Table of Contents

List of Figures, Tables, and Plots:

Acknowledgements

I would like to extend my gratitude to the following people who have made my experience here at Stony Brook constructive, fruitful, and enjoyable. My apologies to those who I will inevitably forget.

To my advisors, Drs. Tom Hemmick and Axel Drees for giving me the opportunity to work and learn with a great group of people and have some fun at the same time.

To Hal Metcalf, for running this great program, and keeping me in line when I start to slack off.

To my committee, Peter Koch, Peter Stephens, and John Hobbs for providing worthwhile advice and being willing to take time out of their incredibly busy schedules for me.

To my fellow researchers here at Stony Brook, Richard Hutter, Richard Lefferts, Bruce Gutschow, Andrzej Lipski, Jason Kamin, Matt Durham, Liz Simola, Greg Wille, Ben Huang, Ben Weaver, and Gaby…Thanks to all of you, I couldn't have done it without you!

To our colleagues at Brookhaven National Laboratory and Weizmann Institute of Science; Craig Woody, Bob Azmoun, Rob Pisani, Sasha Milov, Itzhak Tserruya, and Ilia Ravinovich, you have provided advice, ideas, and assistance without peer.

To my fellow MSI student, Jacob Grimes, for lending a helping hand over these past few years and a great many laughs along the way.

To my parents and siblings, who have provided inspiration, guidance, and support every step of the way.

And last, but certainly not least, to my wife Charlotte, for being patient and supportive through all the long days and late nights that finally saw me through this project.

1.0 Introduction

1.1 RHIC

The Relativistic Heavy Ion Collider (RHIC) at Brookhaven National Laboratory is a unique facility that provides the ability to study matter via collision of heavy ions at extremely high energies. At the moment, RHIC can achieve maximum center of mass energy of $\sqrt{S_{NN}} = 200$ GeV for an Au-Au collision. These collisions allow researchers to examine some of the fundamental properties of quantum chromodynamics (QCD), such as proton spin, color confinement, and the absence of chiral symmetry. At these energies, QCD predicts the existence of a quark-gluon plasma, where matter has become deconfined, yielding a state of free quarks and gluons [5]. This provides scientists with a special tool for studying this rare state of matter, which will help resolve many unresolved questions regarding QCD properties.

1.2 PHENIX

The Pioneering High Energy Nuclear Interaction eXperiment (PHENIX) is a large-scale, global experiment employing approximately 500 physicists and engineers from 54 participating institutions in 13 countries [5]. The PHENIX experiment is a conglomeration of detectors designed to identify the electromagnetic radiation and hard scattering processes that are created in the

QGP. A significant amount of the photons emitted during a collision are seen as muon or electron pairs. In addition to these particles, hard scattering processes result in high multiplicities of charged particles at large transverse momenta. Measuring leptons and photons acts as probes for the QGP phase directly, while studying the numerous hadrons gives information on the later stages of the QGP (hadronization) [4]. In order to measure the production and aftermath of the QGP, PHENIX makes use of a wide range of detector technologies. There are global detectors to identify the collisions, two central spectrometers at mid-rapidity (the hyperbolic angle associated with the frame of reference of the detector) to measure electron, and photon production, and two forward spectrometers for muon measurement [1].

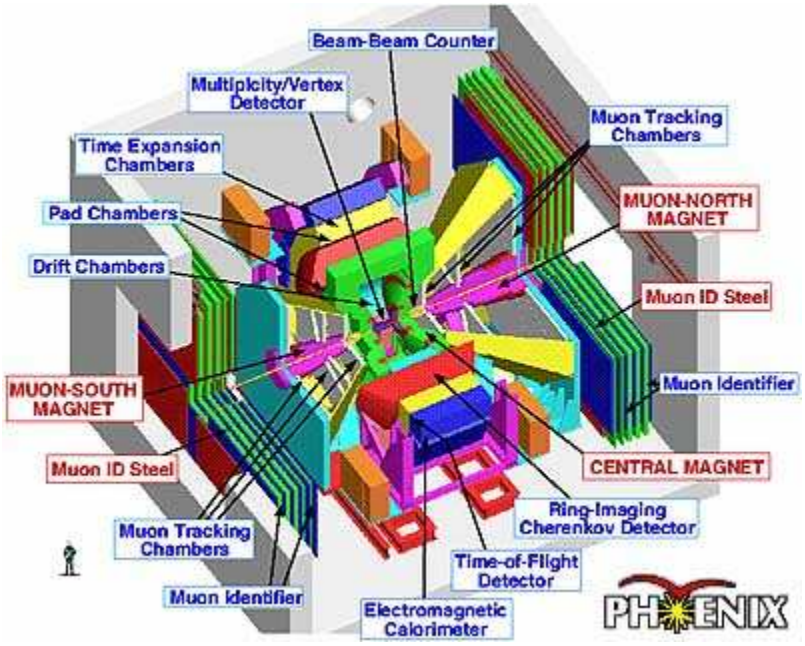

Fig 1: Schematic cutaway of PHENIX prior to HBD installation.

Currently, PHENIX has yielded some interesting results regarding the QGP, but to gain further knowledge about the QGP, the full capability of the detector must be realized. A large-scale upgrade proposal for PHENIX is underway, giving PHENIX the ability to access new observables in RHIC collisions. This thesis is concerned with one aspect of this upgrade, the Hadron Blind Detector (HBD), which will give rise to positron-electron (e^+e^-) pair identification [5].

1.3 A Broad Look at PHENIX and the QGP

One of the defining properties of a QGP is the ability for quarks and gluons to move within the medium independently. This is quite different from the state normal nuclear matter, where matter is bound in pairs (e.g. meson: $quark - \overline{quark}$) or triplets (baryons: three valence quarks). Although the color-charged particles are being released from bound states, the measurement of color charged particles is ultimately a difficult endeavor [1]. This is due to the fact that before measurement, all color-charged particles must recombine. This leads to a possible loss of information regarding the deconfined phase of matter. The main carrier of information in the early stage of deconfinement happens to be in the form of non-color-charged particles, such as real and virtual photons, measured as either e^-e^+ or $\mu^-\mu^+$ pairs. By examining these non-color probes,

there is an opportunity to gain knowledge about the temperature of the early phase of QGP. The technique is not dissimilar from measuring the blackbody spectrum of a UV light source, except that the measurement of these penetrating probes is a far more convoluted undertaking.

Most of the real γ signal arises from π^0 decay, which is not a problem where proven techniques have been able to identify and eliminate the 'decay γ' portion of the signal [1]. The problems begin at low transverse momentum; the sensitivity of the decay γ identification technique is diminished where thermal photons are expected to dominate the signal. Likewise, it is physically impossible to identify $\mu^-\mu^+$ pairs at masses lower than $2m_\mu$. Since these are significant problems to overcome, the e^-e^+ pair becomes the primary probe for examining the temperature characteristics of the QGP (or it's 'blackbody spectrum) [5].

The π^0 meson has a 1.2% branching ratio during the decay to $\gamma + e^-e^+$ $\left(\gamma + \gamma^*\right)$; this is the decay of a pi-zero into a photon and a virtual photon. The main problem is the fact that the production of π^0 in a single collision numbers in the thousands. This leads to e^-e^+ pairs that are 'mismatched' in that the e^+ will be created from one decay process, and the e^- from another. In the case of an ideal detector, this problem would be overcome by recognizing that the pairing was false, and not from the same decay. In the case of Dalitz decay,

which is a low mass decay process associated with the pion, the γ^* is 'virtually real' and contains an invariant mass probability that has a marked maximum at $2m_e$. A pair that has an invariant mass of $2m_e$ has a zero opening angle, which a detector can identify as a 'small opening angle pair'.

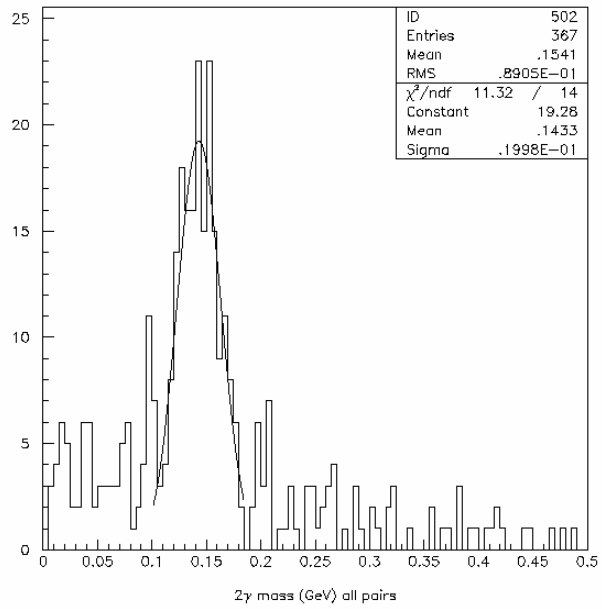

Fig. 2: Dalitz decay peak at $2m_e$, in units of relative intensity vs invariant mass [10].

In the case of the ideal detector, the detector would identify every single e^- and e^+, then it would examine all of them and search for 'small opening angle' hits. The detector would then refuse to identify anything with a small opening angle as a pair with any other particle detected other than themselves.

The largest problem PHENIX faces in this pursuit is the fact that there is a strong magnetic field present in the collision region. The purpose of the field is to enhance the momentum resolution of the present detector systems, but the particles with the lowest *p* are very effectively curled, thereby separating low *p* partners (i.e. Dalitz decays). This scenario also effectively applies to γ-conversions. Simply put, γ-conversion in a vacuum is impossible as it violates *p* and *E* conservation principles. A γ-conversion can occur near large nuclei, as nuclear recoil will no longer violate *p* and *E* conservation within the acceptance of the dectector. Therefore, γ-conversions are a significant source of small opening angle processes and prime candidates for rejection.

1.4 The Role of the Hadron Blind Detector

The specific job of the Hadron Blind Detector (HBD) is to veto e^+e^- pairs, so that our signal to noise ratio is improved, thereby resolving issues with the low mass spectrum at PHENIX. The stated goals for the detector are to achieve a S/B of *10:1* or better at the ϕ-mass, so it must have a single e^- efficiency of *~90%,* it must capture all of the e^- at a p_T *<200MeV/c,* and the pion rejection factor should be on the order of 200 [3].

1.5 Detector Design

The detector has several important parameters that must be met, which is why the detector has had a lengthy R&D period, and the construction and operation of the detector is unique. Presently, the capabilities desired in this detector are a physical impossibility at PHENIX. The detector will be placed close to the collision point, wrapped around the beam pipe. This will mean that the detector will lie within the acceptance of the current detectors and could be a large source of photon conversions; effectively 'blinding' PHENIX with the very object we wish to eliminate [4]. This means the detector must have a low *Z*, to be as transparent and lightweight as possible, and due to the unusual mounting challenges, a low mass detector will be a secondary benefit [6]. This requirement also forces the adoption of using a 'windowless' detector, since space and γ-conversions mean a traditional focused and windowed Cherenkov detector will be physically impossible [6]. The windowless design means that the radiator gas within the detector will also need to serve as the avalanche gas, so it must fill dual-roles. The detector also needs to have sensitivity within the right bandwidth of the UV spectrum to allow effective pair identification [7]. The requirements of the detector and some of the method(s) of implementation are summarized below in Table 1.

Criteria	Reason	Achieved Via
Sensitivity in the UV with high electron efficiency	Appropriate bandwidth for e^+e^- veto measurement	*CsI* (~6eV DL, ~30% QE) and CF_4 (~11.5eV cutoff)
Minimal radiation length	Proximity to collision point and photon conversions	FR-4 honeycomb structure (light mass, lots of empty space) GEM foil detectors (no focusing apparatus, small mass)
Hadron blindness	Needs decent rejection to formulate e^+e^- veto signal	Reverse bias design to eliminate hadron sensitivity while maintaining e^+e^- collection efficiency
Compact Size	Limited space between beam pipe and central arms	Using Proximity focus (windowless), combining avalanche and radiator gas

Table 1: A summary of the HBD design criteria

The basic HBD concept uses two principles to effectively achieve the small opening angle identification premise. It utilizes an extra magnet coil to create a low field region (Treated as zero-field, $r < 50cm$). Within this low field

region, place an electron detector that has the ability to separate a single electron hit from a pair with a small opening angle [9].

2.0 Development and Operation

2.1 Gas Electron Multipliers (GEMs)

The technology that has driven the development of this detector has been the gas electron multiplier (GEM). In general, a GEM is a thin, metal clad polymer foil, typically copper on Kapton™, which is chemically etched with a high density of micron scale holes. GEMs were developed in 1997 by Fabio Sauli at CERN and CERN is the main manufacturer of the GEMs used in research today.

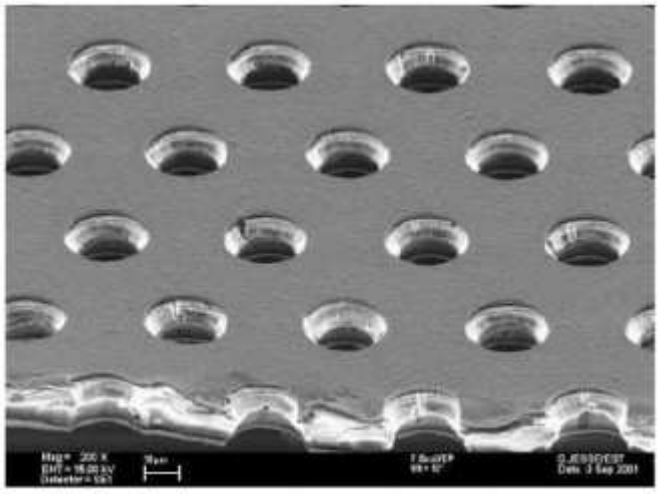

Fig. 3: An electron microscope view of a GEM with 70 μm holes on a 140 μm pitch [11].

When a voltage bias is applied to the conducting surfaces of the GEM, the holes become individual proportional counters – electrons in the gas volume will drift into the holes, multiply in avalanche, and then be transferred into the following region (either to be collected on charge pads, or multiplied further using additional GEMs.) [12]. In the case of the HBD, where tetraflouromethane (CF_4) is utilized, the threshold voltage for gain production is ~300V.

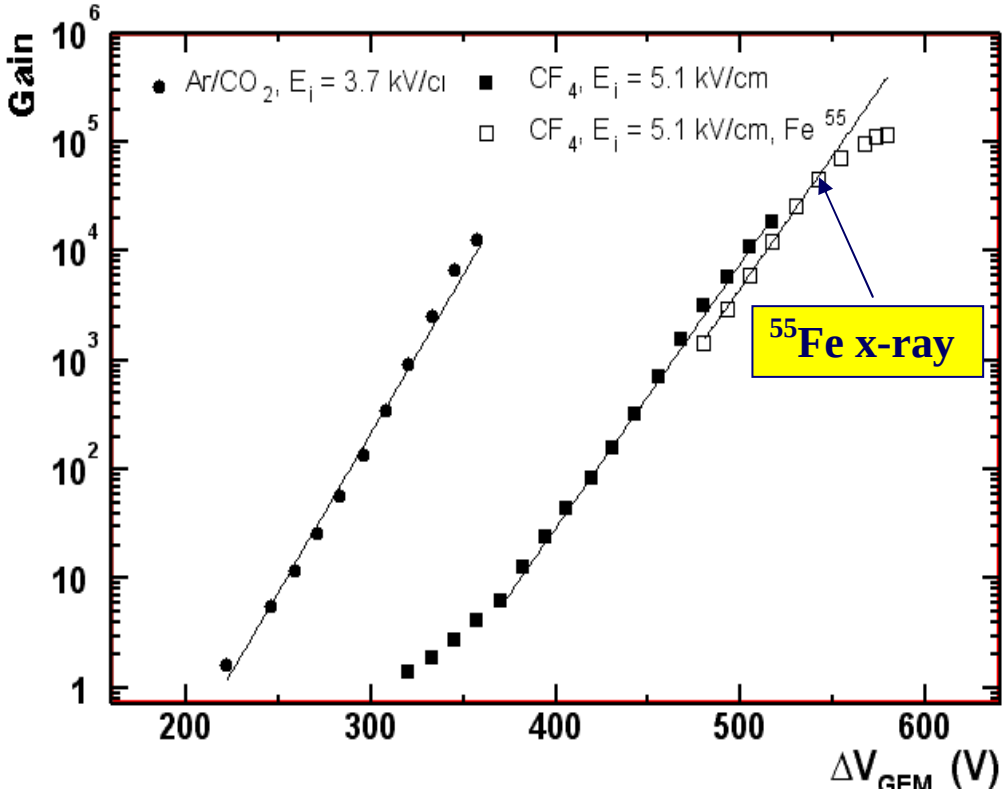

Fig. 4: Gain versus Bias Voltage for HBD gases in kV/cm [13].

GEMs are particularly useful for the HBD in the fact that photon feedback (non-incident photons have difficulty striking the photocathode in the lower stages of gain) is largely suppressed due to their geometric design, so no feedback quenching is necessary in the radiator/avalanche gas as would be the case of some other proposed detector designs (i.e. parallel plate detector).

2.2 Unique GEMs for the HBD

The GEMs being used for the HBD are relatively large in surface area (23cm x 27cm), contain 80μm holes etched at a 140μm pitch, and are divided into 28 strips to prevent catastrophic discharges at the edges of the holes (more on this topic later). The GEMs are also constructed using two different types of metallic foils, Copper (5μm Cu) and Copper-Nickel-Gold (CuNiAu, 5μm Cu, 2μm Ni, 0.1μm Au).

The size of the etched holes, and their pitch, yield a transparency of approximately 80%. This, along with mesh transparency, play a role in determining final quantum efficiency values for our photocathode, they also help determine the gain properties of the GEMs, albeit in a small way. Several factors play a role in the overall gain properties of the GEM foil, some of which are inherent to the foil design (hole size), where others are environmental (gas pressure, gas temperature, purity, etc) [3]. This will be discussed a little further during the commissioning phase of construction.

The Cu GEMs are used in the secondary and tertiary amplifying stages, whereas the CuNiAu GEMs are used exclusively for the photocathode portion of the GEM stack. Standard Cu GEMs were not used as a photocathode layer because *CsI* reacts with the Cu on the GEM, forming CuI, which ruins photosensitivity. CuNiAu is the Mil-spec plating standard, where the Ni forms a 'hard' barrier between the Cu and the Au (CsI deposited on Au can actually seep through the Au surface and still form CuI without the Nickel layer in place.)

2.3 Operating GEMs in the HBD

As stated earlier, the overall premise of the HBD is simple and takes the following form for example. Currently in PHENIX, when e^+e^- pairs are created, one of them will miss the collection of detectors due to the magnetic field configurations used for normal operation. This leads to the reconstruction and statistical nightmare discussed earlier and brought about the discussion of creating the HBD. With the HBD installed, the inner and outer magnets of PHENIX would be configured in such a way to create a low field region in the PHENIX acceptance, this region being occupied by the HBD. With this configuration, during a collision, e^+e^- pairs are created and enter into the detector volume within the low field region of PHENIX [7].

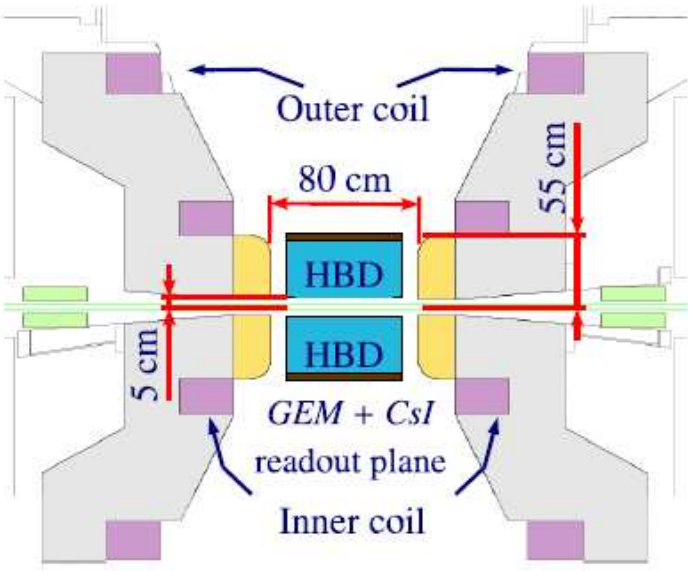

Fig. 5: HBD location within PHENIX [13].

Since there is no presence of a strong magnetic field before e^+e^- pair enters the HBD, neither will curl away from the acceptance of the HBD. This means that the pair will be tagged by the HBD, even if the central arm of PHENIX detects only one member of the pair. These pairs that are identified via the HBD will them be able to be subtracted from the signal in the central arm, effectively removing a portion of false pairs from the statistical data and reducing background by a significant margin [4].

As the e^+e^- pair traverses the detector volume of CF_4, they radiate Cherenkov light. Most of the Cherenkov light passes through the mesh and strikes the photocathode surface. An electron is removed from the *CsI* surface, due to the

absorption of the photon, and this free electron drifts along the electric field lines of the stack. In the drift gap it has a very high probability (almost 1) of being channeled into the avalanche region of the upper GEM [8]. Once the avalanche region captures the electrons, they are multiplied and transferred to the next avalanche region of the middle GEM. The middle GEM avalanches the transferred electrons towards the bottom GEM in the stack, which creates a final avalanche with a gain of ~10^4 to be collected on the readout pads, which are at ground relative to the GEM stacks. The readout pad is coupled to the preamplifier module, which creates the signal to be sent to the PHENIX Front End Module (FEM) that is integrated into the entire data acquisition system for PHENIX [9].

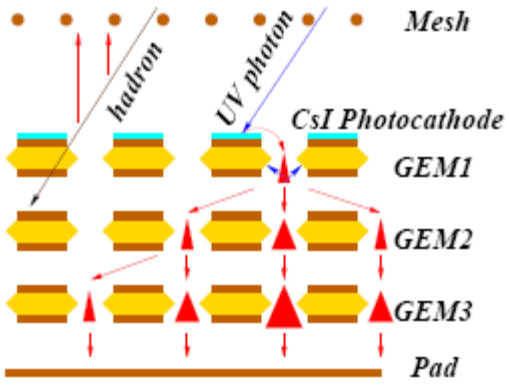

Fig. 6: Schematic representation of the HBD operation [9].

However, the novel design of this detector enhances upon these features of GEMs by incorporating a reverse-bias mode to allow for hadron blindness. Charged particles have plenty of opportunity to avalanche within the design

outlined above, but if a small reverse bias is applied to the mesh above the top GEM, then the charged particle collection efficiency dwindles to a rate that is easily distinguishable from the signal of interest, the e^+e^- pairs. This feature allows us to tune the region (the 'drift gap') between the mesh and the top GEM to be sensitive to photoelectrons, while still rejecting most charged particles within the confines of the detector [2].

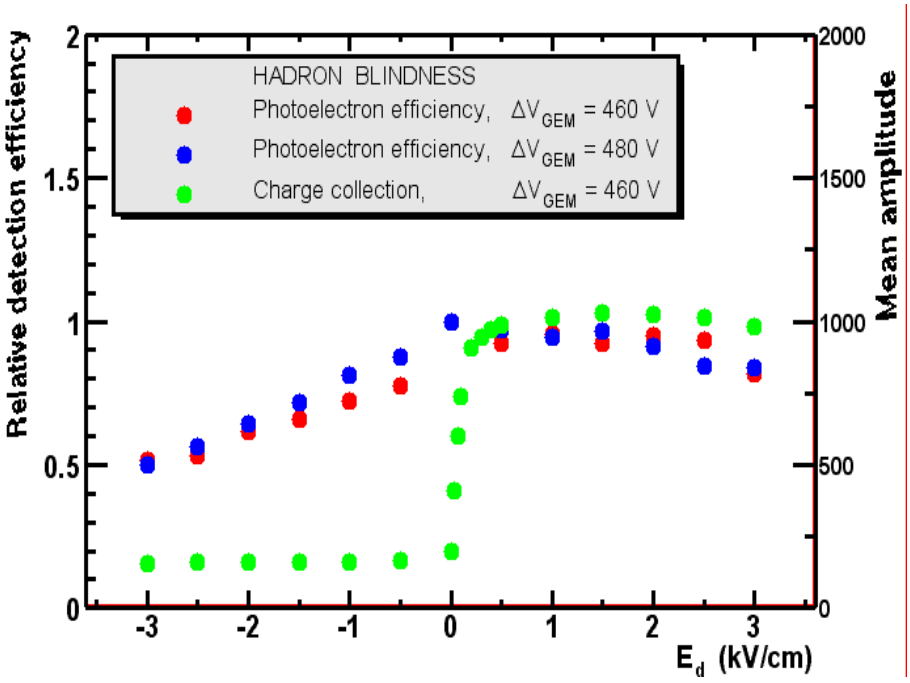

Fig 7: Relative detection efficiency in forward-bias and reverse-bias modes [7].

3.0 Production Facility Development

3.1 Clean Room

Both the HBD Prototype and the final design detector underwent final construction and assembly at Stony Brook University. The production facility is located in part of the target room within the Nuclear Structure Laboratory (NSL). Since GEMs are highly sensitive to dust contamination, it was decided that the PHENIX Drift Chamber (DC) assembly area would be used once again. The DC assembly area is a HEPA filtered clean tent, with a HEPA filtered foyer for changing into cleanroom attire. Prior to installing the production machinery, a complete overhaul of the filtration system was undertaken. The floors were cleaned and polished and a Laminar flow worktable was installed and refurbished.

Fig 8: HBD clean room at Stony Brook.

After the rest of the production equipment was installed, a survey of cleanliness was completed. A MetOne® Particle counter was obtained, calibrated, and placed in successive locations within the clean room, entrance foyer, and laminar flow table. Results of the survey showed that all working areas of the clean room to be better than Class 100. In clean room terminology, a class is denoted by the number of particles ($\leq 5\mu m$) in a given cubic foot of air volume measured. If you have 100 such particles in the specifications listed above, than you can deem the room class 100, an area of class 10 has ten $\leq 5\mu m$ particles per cubic foot per minute, etc. The results of our clean room survey are pictorially demonstrated in Fig. 9**.** The clean room provides all of the major facilities needed for successful production: single-phase *110V* and three-phase *208V* power, house air and water, ample lighting and space.

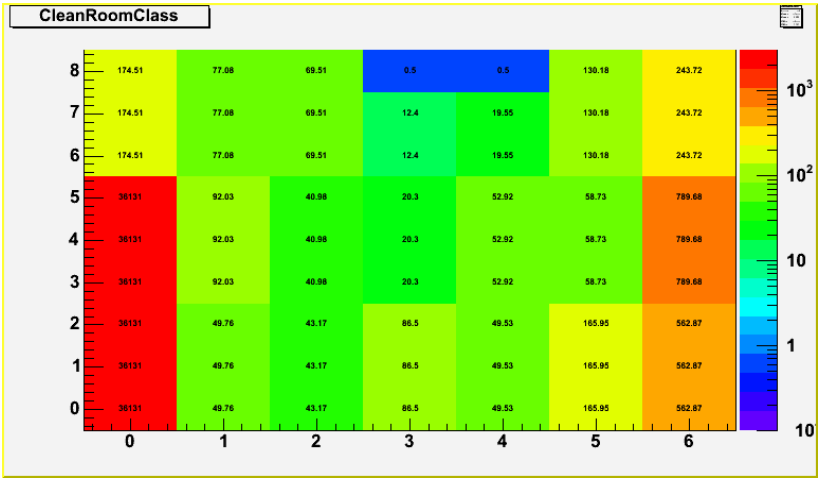

Fig. 9: Clean Room Class measurement map.

3.2 Pre-Production Storage

Beyond clean working spaces, storage space was needed for incoming GEMs while other production procedures were completed. It was decided that storing the non-used GEMs in vacuum was the best solution for two major reasons: 1) Vacuum is a very low dust environment, and 2) Moisture and other contaminants in the FR4/Kapton™ surfaces of the GEM could lead to undesirable characteristics, vacuum would actively 'pump' the GEMs to a cleaner state through outgassing. The vacuum storage system is a stainless steel vessel with a volume of approximately one cubic meter. The vessel is actively pumped through a small turbomolecular pump (Pfeiffer-Balzers TPU 170, 170 L/s), which is backed via a small foreline dry scroll pump (Varian PTS03001UNIV, 250 L/s). An argon refill gas system is employed for when the system needs to be opened to air for GEM retrieval. The storage vessel easily held all prototype, pre-production, and production GEMs and achieves a vacuum of 10^{-6} Torr.

Fig. 10: GEM Vacuum Storage Vessel (VSV).

3.3 Evaporation Preparation and Testing

A laminar flow table (MicroVoid IIc) provided a location for all in-air GEM testing. The table contains a two-stage filtration system, with the final stage being HEPA filtered. As shown earlier, particle surveys show that air within the laminar flow region of the table to be equal to or better than Class 1. This provided the location for almost all in-air GEM operations, such as mounting the GEMs to the evaporation box, and pre-testing.

Fig 11: The laminar flow table.

3.4 Evaporation System

3.4.1 History

The main production phase that the project undertook was the manufacture of the photocathodes for the upper GEM in the stack. Due to time and physical constraints, a unique system was required. Previous *CsI* photocathode production had taken place in a bell jar evaporator in the Chemistry lab of the NSL. This equipment was rejected due to several considerations, namely refurbishing costs, and production efficiency limitations. Next, the Big Mac target chamber was suggested as a candidate for conversion into an evaporation system. Initial design studies and practice evaporations were developed and evaluated, and the project was about to be developed into a real production facility (Sample designs from some of these early studies are included in the Appendix). However, a new opportunity manifested itself just as Big Mac reconstruction was about to take place. The INFN (Istituto Nazionale di Fisica Nucleare) collaboration was custodian of a CERN developed evaporation station at Jefferson Lab in Newport News, Virginia. Dr. Woody and Bob Azmoun had used this facility while participating in some of the fundamental R&D for the HBD and Dr. Hemmick capitalized on the connection. The evaporation facility was lying dormant, and actually blocking further research activities at Jefferson Lab. After some negotiation, it was agreed that Stony Brook would be allowed to become custodian of the evaporation system. A small group from Stony Brook traveled to

JLab and met with an Italian contingent. The system was disassembled and readied for transport to Stony Brook, where it was placed in the clean tent, re-assembled with guidance from the Italian scientists, and then the Stony Brook staff was trained in using the system for successful operations. The evaporator is comprised of two major sections, an evaporation station and a quantum efficiency station. Each section is interconnected via a set of rails that allow the passage of the photocathodes between the area for evaporation and the quantum efficiency measurement area. Both stations share the internal volume of about three cubic meters.

Fig. 12: INFN Evaporator.

3.4.2 Evaporation Components

To achieve high vacuum, the system is compromised of several elements, pumping, control, and measurement. For pumping, the evaporator uses a large dry

scroll pump for rough vacuum (~10 Torr). Once 10 Torr has been achieved, a logic relay in the control system engages the Pfeiffer TMH 1000 SG turbomolecular pump (1000 L/s), which is set to ramp from 0Hz to 660Hz over the period of an hour. This pump can achieve $\approx 1-3\times10^{-6}$ Torr with backing from the scroll pump. Once the turbomolecular pump has completed the starting procedure and is operating at full speed, a large volume cryogenic pump (Edwards CoolStar 1500, driven by CryoDrive 3.0kW) can be manually activated via a separate gate valve relay. With the cryo head at proper temperature and overnight pumping vacuum in the 10^{-8} Torr range can be achieved. The control system has logical control of the measurement and pumping relays, switching automatically between various measuring systems and scales (mechanical gauge > cold cathode gauge > ion gauge). The system also contains a temperature controller that is connected to heating wire, which facilitates bake-out during initial pumpdowns. The standard heating system attempted to use this vessel bake-out wiring to heat the cathodes prior to evaporation. Due to the fact that the vessel is a large stainless steel mass (poor thermal conductor) and the heat from the wires then needed to travel via vacuum (even poorer conductor) to the cathodes within the chamber, the preheating system was deemed insufficient, if not harmful (since you are effectively driving contaminants off of the vessel walls onto the clean, cathode surface.) An externally controlled, more efficient heating system was then developed.

The new, external heating system is a custom-built platinum resistance temperature detector (Omega SRTD-1) based heating system, which is coupled directly to the evaporation box inside the vacuum. One RTD is mounted inside the box, near to the bracket where the GEMs are located, and utilizes an unused portion of the electrical test/quantum efficiency feedthrough. The RTD is connected to a Minco CT16A temperature controller with fuzzy logic, whose outputs are run to another feedthrough that is wired to Minco Kapton™ heating foils attached on the outer surface of the evaporation box. The overall system is a "set and forget" addition that allows independent temperature control of the GEMs themselves while in vacuum.

Inside the evaporation section of the equipment there is provision for four evaporation stations. Copper bus bars couple the electrodes to 4 molybdenum boats via Macor® support structures. The system has been adapted from commercial designs and utilizes watercooled feedthroughs from air into vacuum, which are wired in parallel to the boats

A large AC current is supplied to the system via commercial transformers, and is controlled by the main evaporation control panel. Overall power consumption for a *CsI* evaporation process can be simplified into the following assumption:

$$I_t = 82A @ 630^{\circ}C$$

$$V_t = 12V$$

$$R_t = \frac{V_t}{I_t} = \frac{12}{82} = 0.146\Omega$$

$$P_t = I_t * V = (82) * 12 = 980W$$

The current must be brought up slowly to minimize temperature/resistance fluctuations in the system. Since the boats are wired in series, if one starts to heat and draw less current than the remaining boats, then a temperature mismatch will occur. Since temperature is proportianl to the evaporation rate, the effect of varied temperature must be minimized, as the evaporation rate is an important parameter for a successful evaporation. To combat this issue the system is given two minutes to stabilize between 10A current increases. Due to such variations inherent in the system, we assumed that we could minimize the variations further by basing our evaporation technique on sample mass. Each boat was given an equal mass of CsI and allowed to evaporate completely.

Evaporation thickness is monitored via a commercial system and utilizes PZT mass/oscillation calculations to determine evaporation rate (in nm/s) and total thickness (nm).

3.4.3 Quantum Efficiency Components

The second station inside the evaporator is the quantum efficiency measurement station. This area is comprised of the UV light and gas equipment, current measuring equipment, and a computerized coordinate/data acquisition system to give accurate, reproducible maps of quantum efficiency across the photocathode surfaces. The UV system contained a D_2 lamp, a gas flushed optical box (UHP N_2 gas, to limit UV absorption), bandpass filters, and a mirror control translator. The entire system is mounted to a Conflat® bellows that allows translation of the internal UV apparatus within the quantum efficiency station volume.

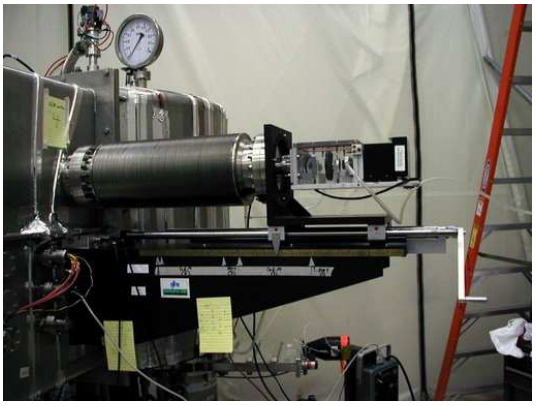

Fig. 13: External view of the QE system (D_2 lamp, optics, bellows, and translator).

The internal section is comprised of a rotating mirror (for selecting UV light onto the photocathode, or the reference PMT), an extraction grid, and a reference photomultiplier tube (PMT) (Hamamatsu R6836) that has been set to

operate in photodiode mode where gain is unity. The reference PMT is wired into a custom external picoammeter that was developed specifically for this role. A wiring harness was developed to facilitate individual GEM extraction currents, which are fed into a second custom picoammeter that has a switching circuit to allow specific GEMs to be measured.

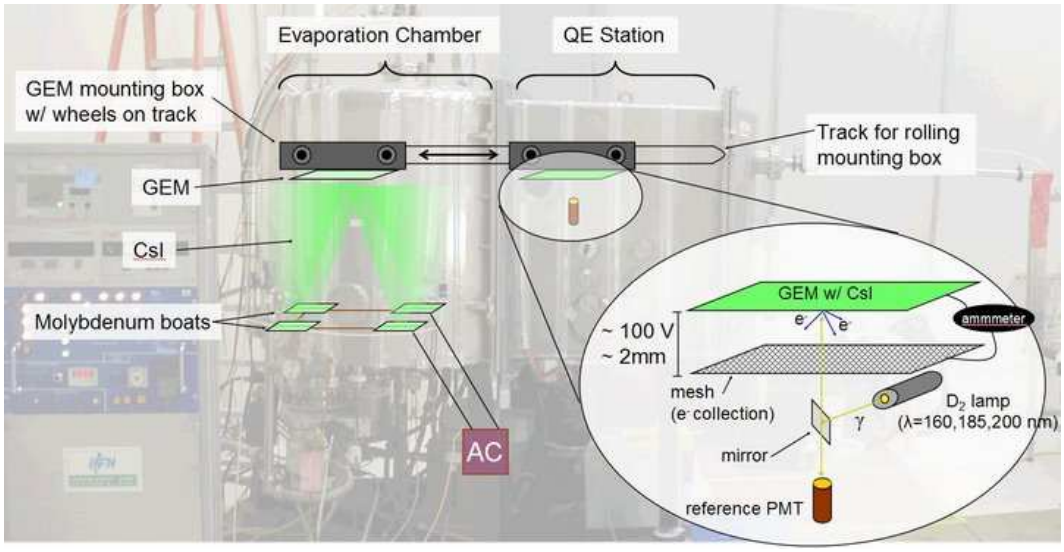

Fig. 14: A graphical representation of the evaporator and internal QE system [7].

Power for the system is provided by 16 *9V* batteries in series to ensure clean bias voltages. The picoammeter outputs are wired into our DAQ system, along with a string potentiometer (a linear resistance device) that provides analog data (0-5V) relating the position of the translating arm.

The DAQ system is a custom developed LabView™ based tool, using generic USB A/D data acquisition hardware that is interpreted by a virtual

instrument (VI). This system allows X and Y mapping of currents on the GEM surfaces, as well as the corresponding reference PMT currents. This data is then placed in a database, and analyzed for quality control purposes.

3.5 Glove Box

It is necessary to have a clean, dry area to dismount photocathodes post-evaporation, and install them and their companion copper GEMs inside the HBD. For this crucial operation, a dry nitrogen glovebox was specified and purchased for installation inside the clean tent assembly area. The glovebox is manufactured by MBraun, Inc and uses a programmable logic based gas recirculation system, has a purgeable antechamber, and 6 workstations for operations related to post-evaporation dismounting, gain testing and mapping, and final installation and testing.

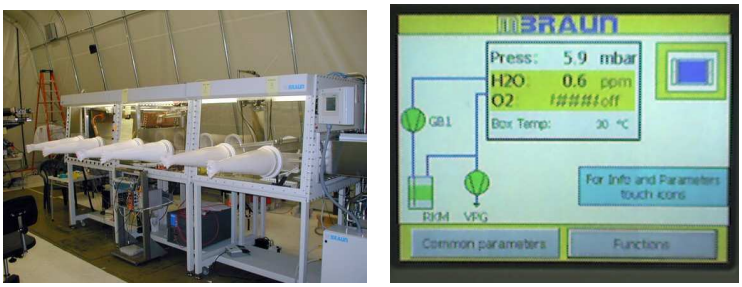

Figs. 15, 16: MBraun N_2 glovebox, PLC controller screen.

The glovebox provides an environment that is low in dust, has a very low latent water content *(<1ppm* water min. *~10ppm* average), and provided adequate

space for assembly and testing needs. Much of the equipment necessary to tackle this project has been developed either in-house by various members of the research team, or by our collaborators at Weizmann Institute of Science (WIS) and Brookhaven National Laboratory (BNL).

Within the glovebox is a gain test apparatus, developed by WIS and modified extensively by our group. It is a pumpable stainless steel vessel that contains a set of charge collecting pads, wired to a breakout panel for individual pad readout. The source used for gain testing is ^{55}Fe, which produces 5.5keV x-rays. The source has a maximum rate (right over a strip/pad) of *~8-10 kHz* attached to a manipulating knob, giving 2π of movement. The vessel is pumped via a diaphragm pump (KNF N726.3ANP, two-stage) and has provisions for gas refilling ($Ar, ArCO_2, CF_4$). A rudimentary pressure transducer allows repeatable gas pressures for test purposes. The pad readout system is completed with a pre-amplifier (Ortec 109A), which is connected via LEMO cables to an amplifier (Ortec 571) and a pulser for calibration. The amplifier output is passed to a Tektronix TDS 1010 oscilloscope for signal monitoring, and to a PC-based multichannel analyzer (Maestro MCA) for data collection. A software layer was written to control the process of gain measurement and gain mapping across the pads to allow for simplified, repeatable operations, and converted data outputs into analysis files.

The final station in the glove box contained half of the HBD vessel itself, sitting inside a frame for detector module assembly.

4.0 Construction Procedures

4.1 Pre-Evaporation

The GEMs arrived at Stony Brook in shipping containers from WIS; the GEMs were removed from the containers, inspected, and sorted into numbered assemblies. Several GEMs were damaged en route, these were removed from the pool of usable GEMs and new assemblies were generated from the remaining pool of GEMs. Other GEMs came without electrical leads attached, or the leads fell off in shipping. These were then placed on the laminar flow table and repaired/completed and returned to the appropriate assembly stacks. All GEMs were then placed in vacuum storage to actively clean them prior to production use.

When production began, four assemblies were removed at a time, with the gold GEMs sent to the laminar flow table for mounting and testing in the evaporation box. The corresponding copper GEMs were placed inside the glovebox, to await the arrival of the complete photocathodes.

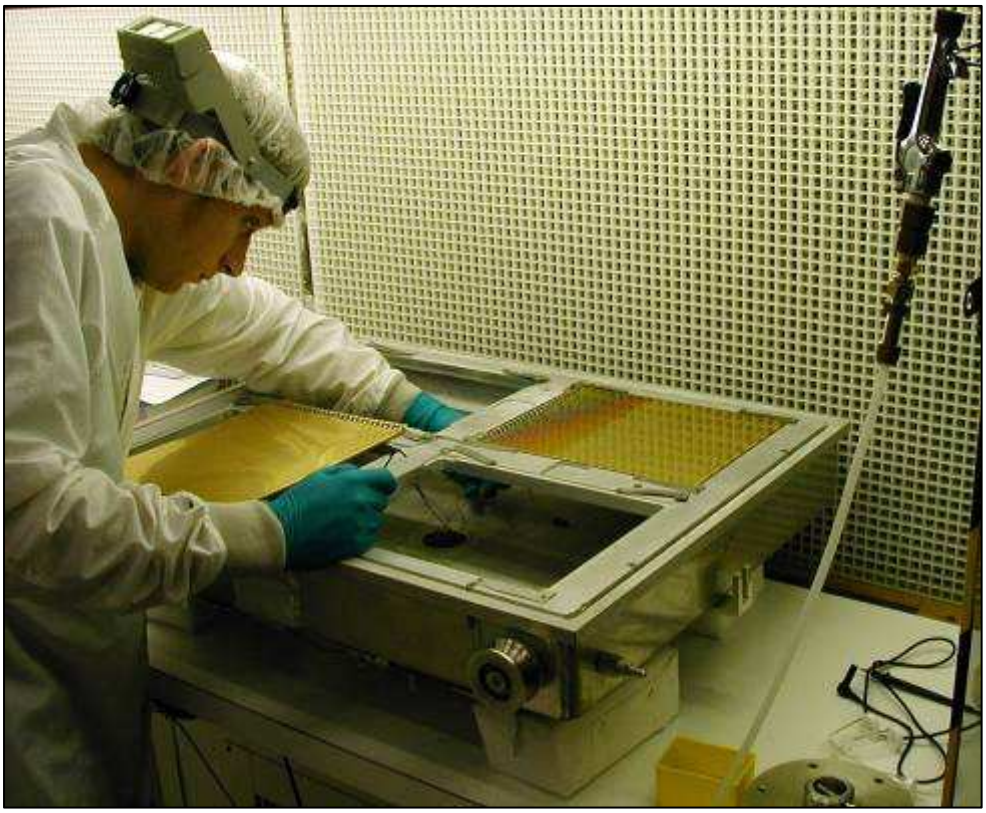

Fig. 17: Mounting the GEMs into the evaporation box.

The evaporation box used to transport the photocathodes came with the evaporator. To mount the GEMs within this box, a custom frame was designed and manufactured to allow four gold GEMs and five test cathodes to be evaporated on simultaneously. The frame also contained pinholes to stow leads and ground connections while the box was in the evaporator. The box is cleaned thoroughly prior to installation, and the five test cathodes (approximately *2cm x 2cm*) are installed. The test cathodes are solid FR4 with a CuNiAu surface to mimic a photocathode (albeit without the holes of a real GEM). These test

cathodes were a provision for absolute quantum efficiency comparisons that take place at BNL, and will be discussed in more detail later. . The box/plate was further modified with the use of a feedthrough to facilitate electrical connections to the photocathodes for post-evaporation testing (quantum efficiency). The feedthrough also managed the connections for the heating system, and served as an external connection for pre-testing the GEMs electrical connections/stability via a high voltage power supply. Prior to sealing the evaporation box the GEMs were energized slowly to a bias of *-400V* in air on the laminar flow table; any current draw over 1-2nA would be noted and investigated as indication of a short on one of the strips.

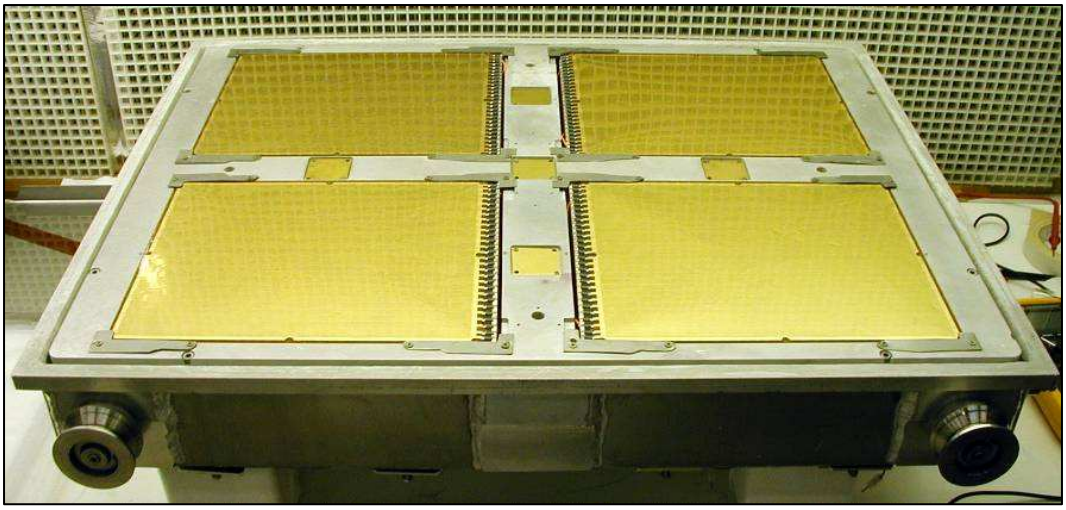

Fig. 18: Ready for testing and then evaporation.

Next, *-100V* was applied to each GEM and then each strip was checked via a multimeter to demonstrate the proper resistance of a strip on the detector. Since the resistors on each strip are rated as $20M\Omega$, we can measure the input current of the circuit via the high voltage supply. A proper, clean, function strip will draw $1-3\mu A$ as the bias voltage is increased. Since the meter is also a $10M\Omega$ resistance to the circuit, if all is functioning properly, we should measure $\frac{1}{3}$ of the original voltage along the strip, or *-33V*. A strip suspected of being shorted or dust contamination would be thoroughly cleaned via compressed *Ar*, to dislodge any dust in the etched holes, and rechecked. Only GEMs that had 100% strip functionality proceeded to the evaporation to become photocathodes. With pre-testing completed, the evaporation box would be sealed and transported to the evaporator.

With the photocathodes ready for evaporation, final preparations to the evaporator needed to be made. The *CsI* comes in raw crystalline rods, approximately *2cm x 2cm x 10cm*. Prior experience had shown us that a mass of approximately *0.80g* would yield a target thickness of *~350nm* if evaporated fully. Raw *CsI* crystals were placed in an *Ar* filled glovebag located in the Chemistry lab of the NSL, where they were cut, measured to the appropriate mass, and placed into sealed vials. The sealed vials were then taken to the cleanroom where they awaited the final stages of evaporation preparation. The evaporation box gets

placed inside the evaporator, the lid is affixed to a central post that can raise and lower the lid, and the lid clamps are removed.

Fig. 19: Inside the evaporator, preparing for evaporation.

Following the evaporator box installation, the wiring that connects the GEMs to the quantum efficiency system, RTD, and Minco controller/heaters is connected. The wiring harness is checked for proper connections and then the grid for the quantum efficiency apparatus is connected. The vials of *CsI* are distributed to each *Mo* boat, a shield is placed in front of the grid/PMT system to prevent *CsI*

contamination, the lid is lowered to its evaporation position and the systems is inspected, cleaned, and sealed for pumpdown.

4.2 Evaporation

As described earlier, the system is highly automated, but there are a few levels of manual control that ensure high quality, reproducible results. One such factor is the residual gas analyzer (RGA) built into the system. The RGA is a Prisma QMS series mass spectrometer developed by Pfeiffer Vacuum Technologies, and is a useful tool in determining vacuum quality and composition. The system is comprised of the mass spectrometer and a PC running Pfeiffer QMS200 (ver.4) software for data logging and display. When the evaporator has achieved 10^{-5} Torr of pressure, the Prisma system is turned on and RGA logging is started to examine the properties of the vacuum. At initial start up, the quantity of major residual gas molecules is on the order of a few nanoamperes (equivalent to ~10^3 mol/m^3) with the most noticeable peaks at the masses for N_2 and H_2O water.

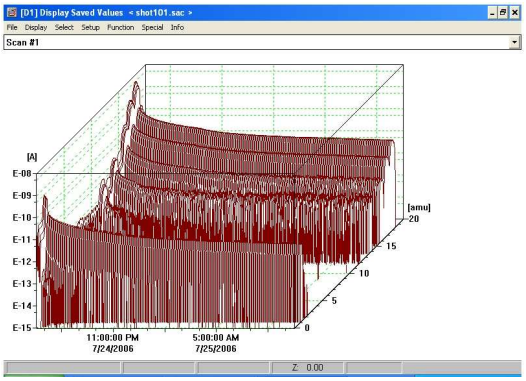

Fig. 20: RGA scans (Lower masses, from intial scan through ~12h).

Once the turbomolecular pump is fully on-line, the cryopump is opened to the vacuum and a noticeable drop in residual gas can be monitored. Online monitoring takes place throughout the remainder of the evaporation period, which contains a minimum of 24 hours for pumpdown. Vessel baking is turned off for at least an hour prior to actual evaporation to remove the possibility of vessel surface contaminants interfering with the evaporation. Prior to actual evaporation, the RGA is consulted to determine if water levels have reached the typical value of several picoamperes

Actual evaporation is a rapid process, beginning with a template to record evaporator parameters, and readying the evaporation circuit. The electrode power supply is turned on and set to 12*V*, the thickness monitor is activated and zeroed, and the current control is set to zero. Next, the current control is gradually increased by *10A* steps every two minutes, to ensure stable current flow and thermal equilibrium in the circuit. Once *~75A* have been reached, the thickness

monitoring begins to demonstrate thermal evaporation of the *CsI* by displaying a rate and a thickness. The current control is subtly increased to attain a rate of *~2nm/s*, usually resulting in a final current of *~82A*. While this is occurring, the RGA system shows the presence of *CsI* in the vacuum with corresponding peaks at the correct masses.

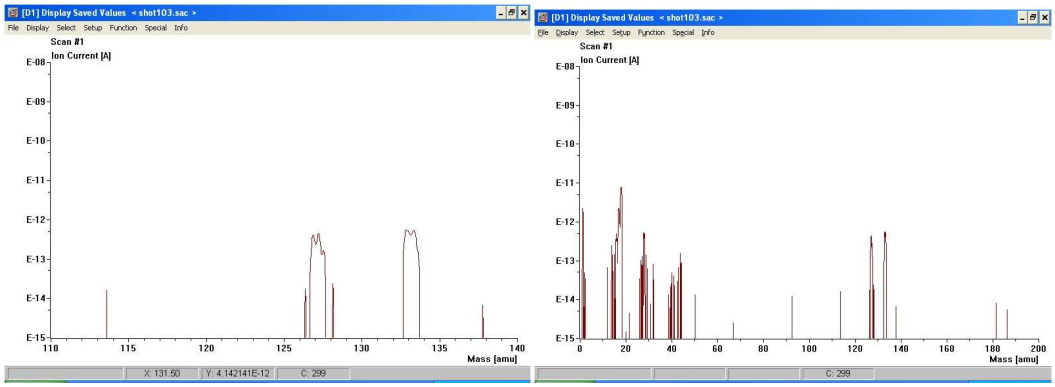

Figs. 21, 22: Zoomed in where the *Cs* and *I* masses are visible, and at full scale.

This procedure is maintained until the thickness monitor shows the rate to gradually decrease to zero. Then the system is left at peak current for two to three more minutes to ensure that the *CsI* is fully evaporate from the *Mo* boats. Now, the current control is turned back down to zero and the power supply turned off. The applicable parameters (rate, final thickness, final current, etc) are recorded and the thickness monitor is turned off.

The next stage is to allow the *CsI* to fully crystallize on the photocathodes, a process that is completed in vacuum, with no additional heating and takes 6-12 hours. This process was developed via trial and error after building a reliable quantum efficiency apparatus. During this time, there is no user interaction within the system except for monitoring the RGA logs and preparing for quantum efficiency measurements of the newly completed photocathodes.

4.3 Quantum Efficiency

Quantum efficiency measurements give a relative comparison for quality control purposes. The system built into the evaporator is not an absolute system, but rather a relative quantum efficiency to compare all four production GEMs. Both our in-house system and our absolute measuring system will be described here. To obtain absolute reference values, a system was devised to use our capabilities in conjunction with equipment available at Brookhaven National Laboratory. At Brookhaven there exists a system to test small GEM based photocathodes for research and development work. The sample holder in this system can hold GEMs that are two centimeters square, so we developed 'dummy' photocathodes that are made of gold plated FR4. These dummy photocathodes mimic the surface of a GEM perfectly, with the exception of the 20% transparency of a real GEM (due to the etched holes). This factor of

transparency is applied to the final quantum efficiency figure to accurate gauge absolute quantum efficiency.

The dummy photocathodes are mounted into the same frame that holds the real photocathodes for evaporation. All photocathode surfaces are at the same reference plane to ensure that thickness variations will be negligible. The dummy photocathodes are placed in the center of the frame to account for the farthest distance from the evaporation point, thus giving us a lower boundary for quantum efficiency within our system. Once an evaporation is complete, our in-house measurements are done only on the production size GEMs, and then when those GEMs are removed for installation, the dummy photocathodes are removed from the frame, sealed in a vacuum transport box and moved to BNL where the absolute measurement is completed and filed according to evaporation.

The BNL system is automatic after the sample has been installed, pumped on, and the D2 light source has been turned on and allowed to stabilize for approximately an hour. The system is comprised of a VUV monochromator (Jobin Yvon H20, 115-200nm), which contains the D2 lamp (Hamamatsu L7293, 115-320nm), monochromator optics, *LiF* beam splitter (105nm cutoff), lamp intensity PMT (PMT-0, Hamamatsu R1460) and a LiF output window to the detector box. The detector box contains an absolutely calibrated PMT (Hamamatsu R6836, operated in photodiode mode, gain = 1), the sample mesh/photocathode and a rotating UV mirror. The mirror then directs the light at

either the sample mesh/photocathode or the second PMT with collimators in front of each target to ensure comparable solid angles. The current is measured for each case, logged in LabView, and then the monochromator indexes to the next wavelength. The system is schematically represented in Fig. 25.

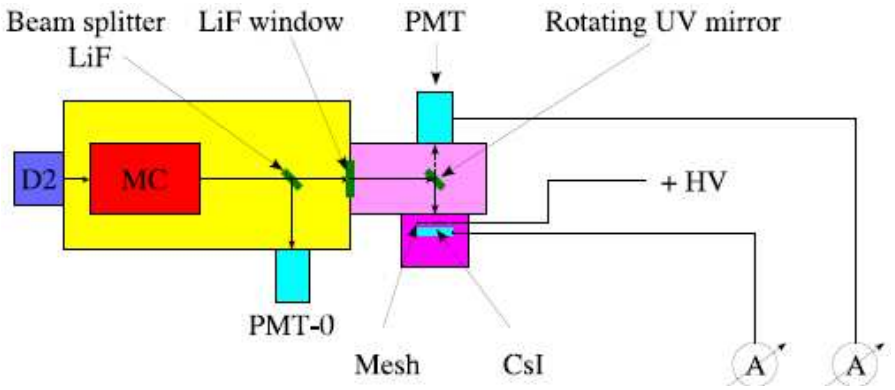

Fig 23: Schematic of the BNL quantum efficiency apparatus [2].

The system repeats this process in 2nm wavelength steps between the ranges of 120 to 200nm. Typical results are shown in Fig. 26, as well as a comparison with other measured values from WIS.

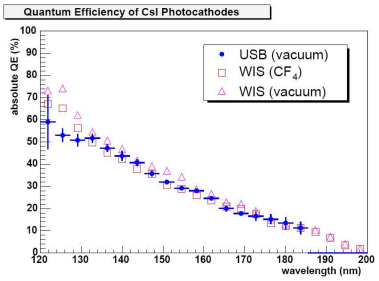

Fig 24: Typical QE measurement on BNL system [9].

The in-house quantum efficiency measurement system is a modified version of the system we inherited with the evaporator. As described earlier, it consists of a deuterium light source (Hamamatsu D7860), an optical box with a filter wheel (165nm, 180nm, 205nm), a movable bellows, a rotating UV mirror, an extraction mesh, and a reference PMT (Hamamatsu R6836, operating in photodiode mode, unity gain). The system is wired into a custom VI in LabView that allows x and y position to be mapped with a reference PMT current (dark and light) and cathode current (dark and light), via a custom-built picoammeter.

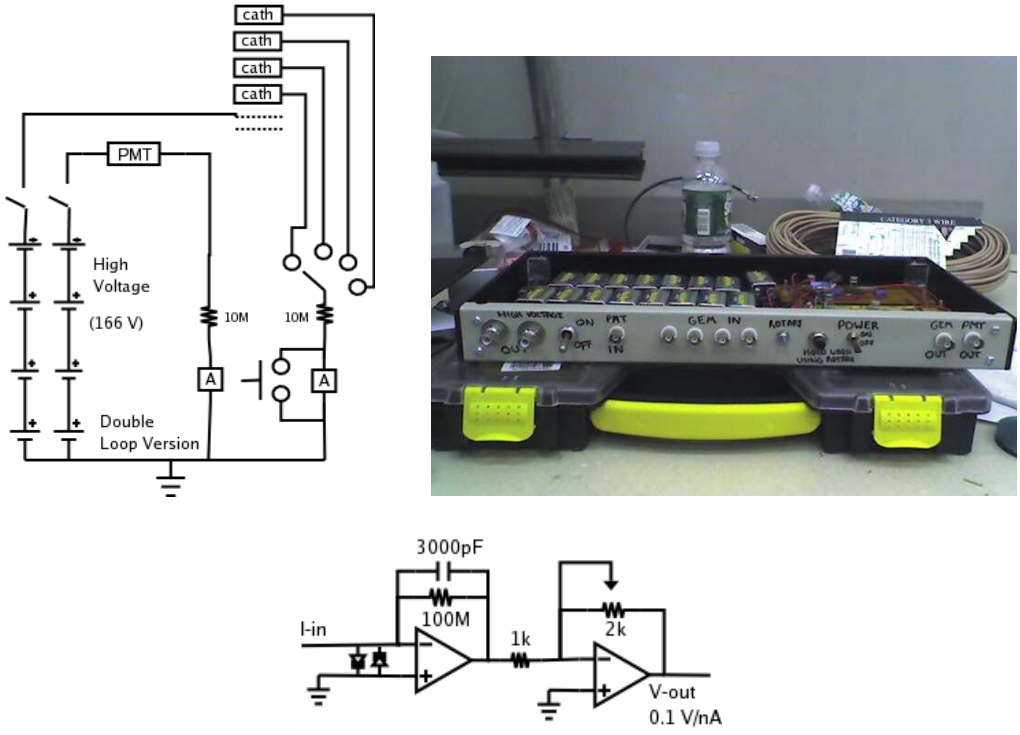

Figs. 25-27: The dual picoammeter concept used for HBD QE, an external view of the picoammeter, and the picoammeter schematic.

UHP N_2 is flowed through the system during lamp warm up, which takes approximately an hour. Three scans (Y) are taken across the X direction of each GEM, one direction is a light scan on the photocathode (simultaneously measuring dark current on the PMT), then the mirror is reversed, and the scan is repeated in the opposite direction (light on PMT, photocathode dark current measured concurrently). The relative quantum efficiency is then determined as follows:

$$QE_{cathode}(\lambda) = QE_{PMT}(\lambda) \times \frac{(I_{cathode} - I_{darkcathode})}{(I_{PMT} - I_{darkPMT})} \times \frac{1}{0.8}$$

This is given by the fact that the QE_{PMT} is well known for the λ we are measuring at, and the 0.8 is to account for the fact that 20% of the GEM surface is transparent. With this setup we can quickly get a picture of the quality of the evaporation, as well as give us a comparison to other published values for *CsI* QE. The other main advantage of the in-house QE system is that it gives a picture of the QE across the surface at each end of the GEM and in the middle as well. The string potentiometer keeps track of the x-position (precision of *0.005V, 0-5V* over 0.5m), and the y-position is manually adjusted and logged in the software, along with mirror position.

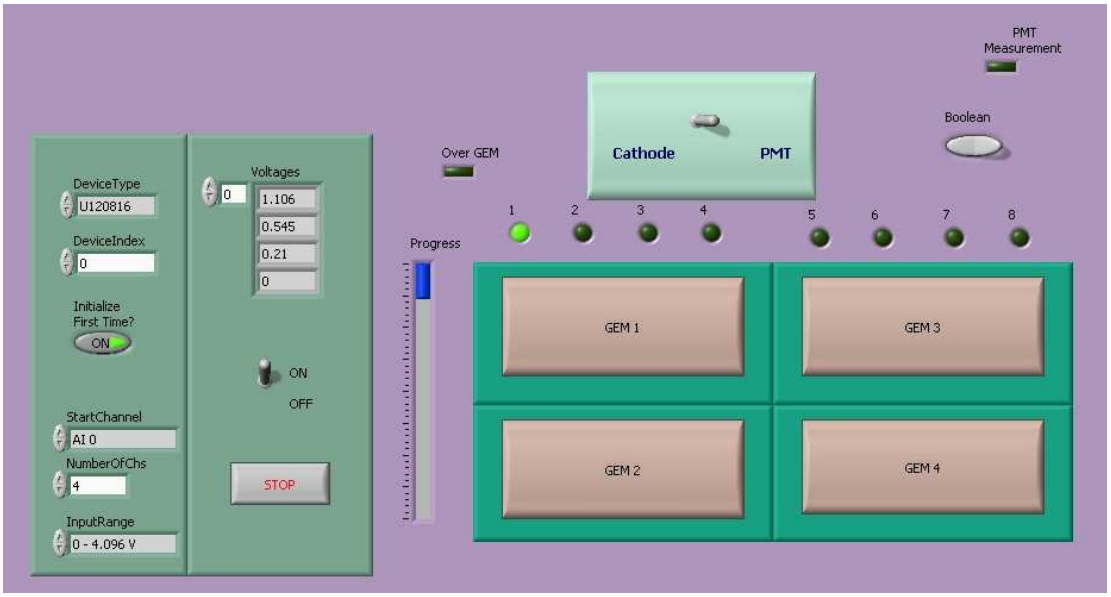

Fig. 28: LabView QE DAQ interface.

After the twelve scans are completed, the data is compiled into files, databased and examined for any evidence of poor quality or damage. (See Appendix for production data). Upon successful examination, the system is shut down and the GEMs return to the first station within the evaporator for the let-up procedure.

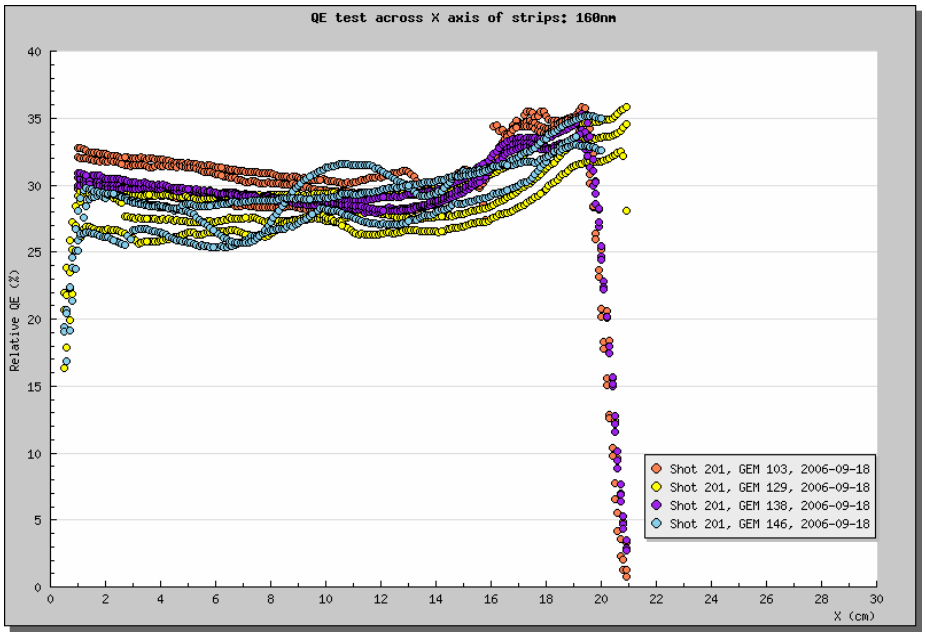

Fig. 29: Example of a typical in-house QE measurement, relative QE % vs x - position.

4.4 Post-Evaporation

Following a successful evaporation, the GEMs now have a sub-micron coat of *CsI* on the surface. This means that they are both dust and moisture sensitive. Therefore, our transport to the assembly area must remain airtight for the 5 minutes of transport time. The evaporation box has a rubber o-ring machined into the outer lip of the box. There is also a lid that is mounted to a mast within the evaporator. The vacuum system and RGA are turned off and the vacuum chamber is then vented with *Ar*. Once the system has almost reached atmospheric pressure, the mast inside the evaporator is raised and the lid is pressed against the o-ring surface on the box. To fix the lid to the box requires

manual intervention after the system has reached atmospheric pressure, at which point the chamber is opened, and a person must enter the volume and affix clamps on the outer surface of the lid. Minor contamination can result at this point if the lid isn't driven onto the box correctly, so tabs were used to guide the lid on correctly and the mast is held in place to hold the mass of the box down onto the lid/o-ring surface. Once the clamps are in place, the mast is lowered and the cabling into the heater/QE measurement equipment is decoupled. The box is then rolled out onto the transport lift, lowered, flipped over, and transported to the glovebox antechamber. The box is then rolled into corresponding rails in the antechamber, sealed, and then the antechamber is purged with nitrogen gas for ten minutes to remove contaminants from the transport process. Once the antechamber purge is completed, the inner door to the glovebox is opened and the evaporation box is rolled into the first glovebox workstation for dismounting and test preparation.

4.4.1 Evaporation Discussion:

The evaporation techniques were developed through advice of our Italian colleagues, prior experience, and empirical observation. The system underwent major modifications in several key areas to make evaporations of consistent and high quality. Much of the experimental effort was focused on using the system, logging results, improving upon several factors (vacuum quality, heating techniques, QE measurement techniques, installation/removal protocols) that by

the time production began, every member of the evaporation team (the author, graduate students Jason Kamin and Matt Durham, and advisor Dr. Tom Hemmick) had experience and insight in the methods used for successful evaporation.

4.5 Glove Box: Testing and Assembly

The photocathodes are located inside a sealed evaporation box within a clean, low moisture environment (glovebox), the lid clamps to the evaporation box are removed, and the lid is pulled up out of the way. The four photocathodes are taken off of the evaporation frame and join their corresponding copper GEMs to await gain tests. The five dummy photocathodes are now removed, inserted into vacuum transport, and sent to BNL for the aforementioned absolute quantum efficiency tests.

Fig. 30: Removing *CsI* coated GEMs from the evaporation box, while inside the glovebox.

4.6 Gain Tests

Photocathodes and their companions are next moved to the second station in the glovebox, which contains our gain test station. The GEMs are set inside the vessel, stacked in their correct order (two coppers for bottom, middle of stack, Au photocathode, and mesh).

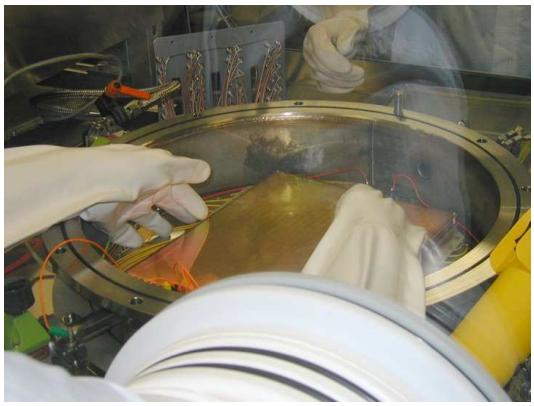

Fig 31: Stacking GEMs into the gain test station.

During stacking, initial testing takes place. First the GEM is tested for capacitance, this ensures electrical continuity with the outside world and gives a first order approximation to GEM condition, and a healthy GEM should read *~28-29nF*. The physical layout of the GEM mimics a parallel plate capacitor, which we have divided into 28 segments to minimize the stored energy $\left(E = \frac{1}{2} C V^2 \right)$ within the GEM, high stored energy can lead to catastrophic discharges. Since we have two conducting planes (Cu or CuNiAu plating) with an

applied potential (bias voltage, allowing avalanching) separated via a dielectric (Kapton™), the GEM can be considered a parallel plate capacitor with a capacitance determined by:

$$C_{strip} = \varepsilon_{kapton}\left(\frac{A_{strip}}{d_{kapton}}\right)$$

$$\varepsilon_{kapton} = 3.9\times\varepsilon_0 = 3.45\times10^{-11}\frac{F}{m}$$

$$A_{strip} \approx 0.75cm\times27cm \approx 20cm^2 \approx 0.002m^2$$

$$d_{kapton} \approx 70\mu m \approx 7.0\times10^{-5}m$$

$$C_{strip} = 3.45\times10^{-11}\frac{F}{m}\left(\frac{2.0\times10^{-3}m^2}{7.0\times10^{-5}m}\right) \approx 1nF$$

$$1nF\times28strips \approx 28nF$$

With a successful capacitance test, the GEM is then taken to a *-100V* bias (bottom side shorted, *-100V* on top side) and each strip is checked for shorts (*~33V* per strip for OK strips). This test is the same as the test applied to the GEMs for pre-evaporation testing, except that now each GEM is tested, not just the photocathode GEMs.

Fig. 32: Testing voltages on each strip.

Upon successful strip testing, the GEM is then taken up to *-550V* in the N_2 environment to test stability. Often the system will trip along the way (Bertan HV power supply, model 1746, set to trip at 80% of current scale, the maximum current setting is typically $10\mu A$, thus the system will trip at $8\mu A$). When this happens, the HV system is turned off and the process is restarted until the full *-550V* can be held stably. At this time, if any current is measured in the system, it is noted and the resistance is calculated to determine if it is due to a short between the top and bottom layers. If the current rises and then drops precipitously, we claim that we have sparked dust out of a hole in the GEM, which could lead to a trip or require higher voltages to clear. This is tested on a case-by-case basis and is random. Once this conditioning step has been completed successfully, the GEM is declared fit for further testing, and the next layer in the stack is placed in the test box, and tested with the same procedure until the stack is fully built. Once the system is wired up, the lid is lowered and the volume is pumped down to 50-60 mbar. Then the volume is flushed with $ArCO_2$ mix, up to atmospheric pressure. This is pumped out down to 50-60 mbar again and refilled to atmospheric pressure with $ArCO_2$ again. Now the entire stack is powered up via a resistor chain hooked into a second channel of the Bertan, set with a higher current setting since the resistor chain will draw a non-trivial amount of current as higher voltages are reached. Once operating voltages have been reached, a measurable

Fe^{55} peak can be seen on the oscilloscope, with two distinct peaks of differing amplitude (Fe^{55} peak and an $ArCO_2$ escape peak, only visible in $ArCO_2$ measurements.)

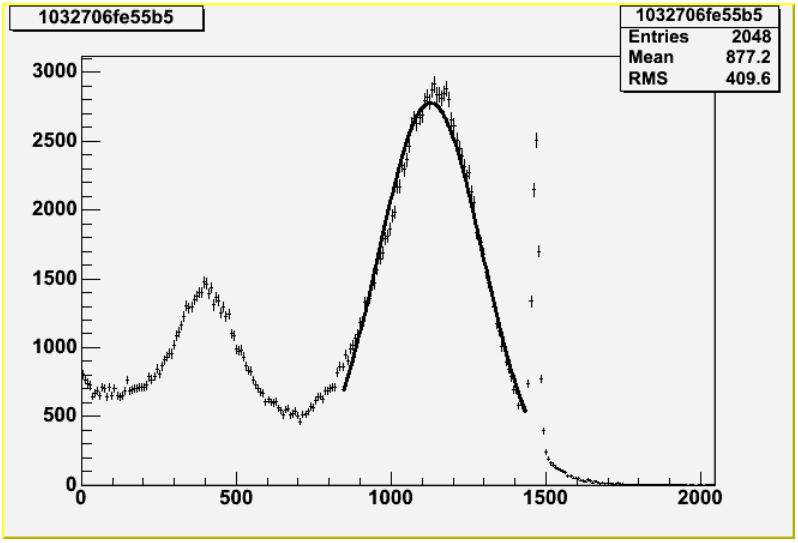

Fig. 33: Fe^{55} peak with a $ArCO_2$ escape peak and a calibration channel.

This occurs around a net voltage of -2500V, which yields a bias voltage of approx. -300V per layer of the stack. Voltage is then increased to the test value of -2680V and the Fe^{55} source is adjusted for maximum rate over our first test pad (arbitrarily chosen to be C2). The appropriate software parameters are logged (pressure, temperature, rate, pad#, voltage, etc) and the software then logs the gain of the system over a period of 20 minutes. Next, the software switches over to mapping mode and directs the users to move the patch cable to the first pad in the map, A1. The source is maximized over this pad and then data is collected for 1 minute. The system automatically prompts the users to continue moving through

all 56 pads for one minute maximized measurements. Once the map is complete approximately an hour later, the system then refers the users back to pad C2 for another 20 minute maximized gain versus time study, which can then be used to calibrate the data taken over the mapping period. Once the software has completed taking data, the files are automatically post-processed and sent to be databased and analyzed further. The system is de-energized and the users can pump the working gas out of the volume, and refill the chamber with the glovebox atmosphere. The lid is removed and the stack pulled out, transferred over to the next station for HBD installation and the next stack is built and tested according to the previous procedure.

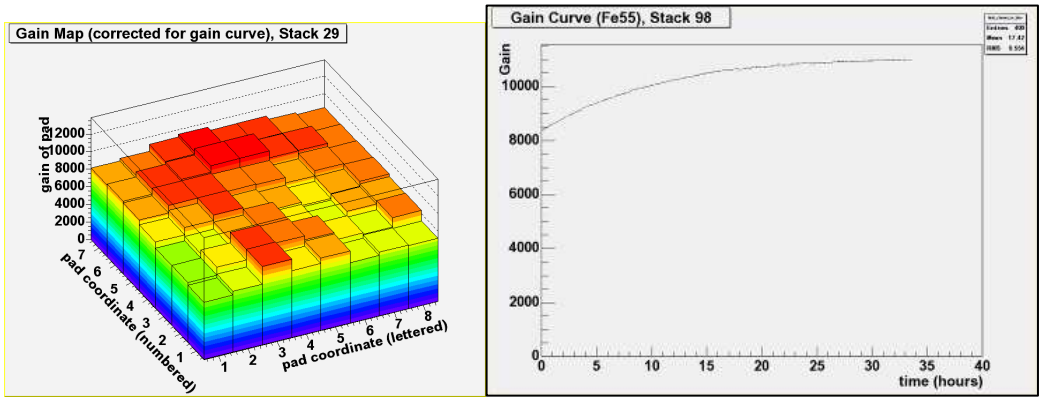

Figs. 34, 35: An example gain map and curve taken from production data.

4.7 Final Installation

Assembly of the GEMs into the detector vessel is a delicate and awkward procedure, we developed a cradle and some specialized nut driving tools to ease

the process by extending reach and letting us angle the detector to make the furthest positions accessible. Building the stack follows the same procedure as the gain test, only without the voltage tests, so just a capacitance test is used to determine electrical continuity and initial damage checking.

Fig. 36: Testing for continuity and capacitance.

This procedure is continued until all stacks have been built, and then they can be fastened down to the pad surface via nylon nuts (which cause interference to the adjoining GEM stacks is placed on the posts before all the stacks are built.)

Fig. 37: Tightening down the GEMs within the vessel.

With a fully completed module ready to go, capacitances of every GEM are checked a final time, and an AC signal is injected into each GEM to determine GEM condition including the now-connected high voltage divider chain. The concept behind this test is a simple one. Since the GEM can act as a capacitor, we know that it has an impedance of $\left(\frac{-j}{\omega C}\right)$, so if a resistor and frequency are chosen such that $\left(R = \frac{1}{\omega(29nF)}\right)$, the circuit will behave as a voltage divider if continuity exists. This is represented by an attenuation of the AC signal displayed on the oscilloscope. If a GEM lead is damaged, then the signal displayed on the oscilloscope will be the unattenuated AC signal. If a $100k\Omega$ resistor is chosen,

the measured V_{out} in the circuit should be approximately $\frac{1}{2}$ the V_{in} if input frequency is calculated as:

$$\omega_{cutoff} = \frac{\sqrt{3}}{RC} = \frac{\sqrt{3}}{(1\times10^{5}\Omega)(2.9\times10^{-8}nF)} \approx 600\frac{rads}{s} \approx 95Hz$$

So at approximately $95Hz$ our signal should hit the cutoff and we can visually determine that continuity exists. This test is also effective at finding small shorts, which did not occur (Dead short = full V_{in}, proper circuit = $\frac{1}{2}V_{in}$, small shorts = V_{in} something in between dead short and proper circuit.)

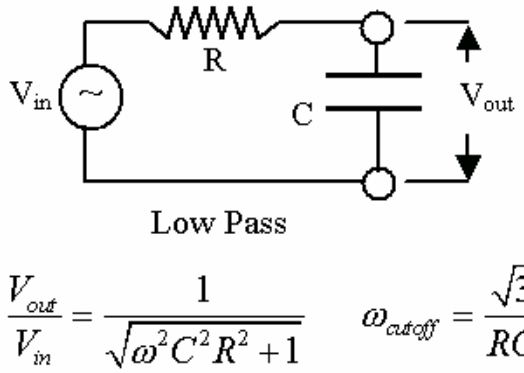

Fig. 38: Final continuity check circuit schematic.

With all tests completed and declared successful, the sides of the detector need to be reinstalled and the glovebox prepared to be opened to remove the completed detector arm. All of the gas ports are sealed on the detector volume to prevent a pressure differential between the detector volume, the glovebox, and the

world at large. The glovebox is shut down and one of the windows is removed to facilitate the removal of the detector within the assembly framework.

4.7.1 Final Assembly Discussion:

The final assembly process was not without pitfalls, the precision of the threaded posts that held the GEMs to the HBD pad plane allowed little room for error. Working in the glovebox for long periods of time lead to mistakes being made, where damage occurred to a mesh or two, leads were lost and required in glovebox repairs, and lots of trial and error was necessary for learning how the GEMs and nuts would work most efficiently (creation of tools and techniques). Testing procedures were modified to account for the presence of the high voltage divider network, and the fact that the leads were plugged into the bus bar. Given the scale of the work, and the manpower involved, the first arm served as a valuable lesson and made the construction of the second arm take half the time.

5.0 Commissioning

5.1 Gas System

Upon retrieval of the detector from the glovebox, the detector needs to be removed from the assembly frame, as quickly as possible, as the volume of gas inside the detector will quickly saturate with water outgassing from the Kapton™ surfaces. As soon as the detector is secured outside of the assembly frame, it is hooked into a mobile gas station that supplies gas ($Ar, ArCO_2, CF_4$) through an Oxisorb™ canister. The gas is then distributed through the detector volume and the output is analyzed for water and oxygen content using GE Panametrics ™ sensors, hardware, and software. This gas supply system is basically a simplified version of the permanently installed gas system used for detector operation in the PHENIX experiment hall.

Since water is one of the main sources of UV absorption in the working range of the detector, strict limits must be achieved (See Figs. 39-41); otherwise the photocathode will not provide the necessary signal to operate in full gain. To obtain ~95% of the desired Cherenkov signal, water levels must remain below 15 parts per million (ppm). Oxygen also affects transmittance in the radiator gas, but it also serves as an indicator of leaks within the closed system. Oxygen levels need to remain below 10 ppm [4].

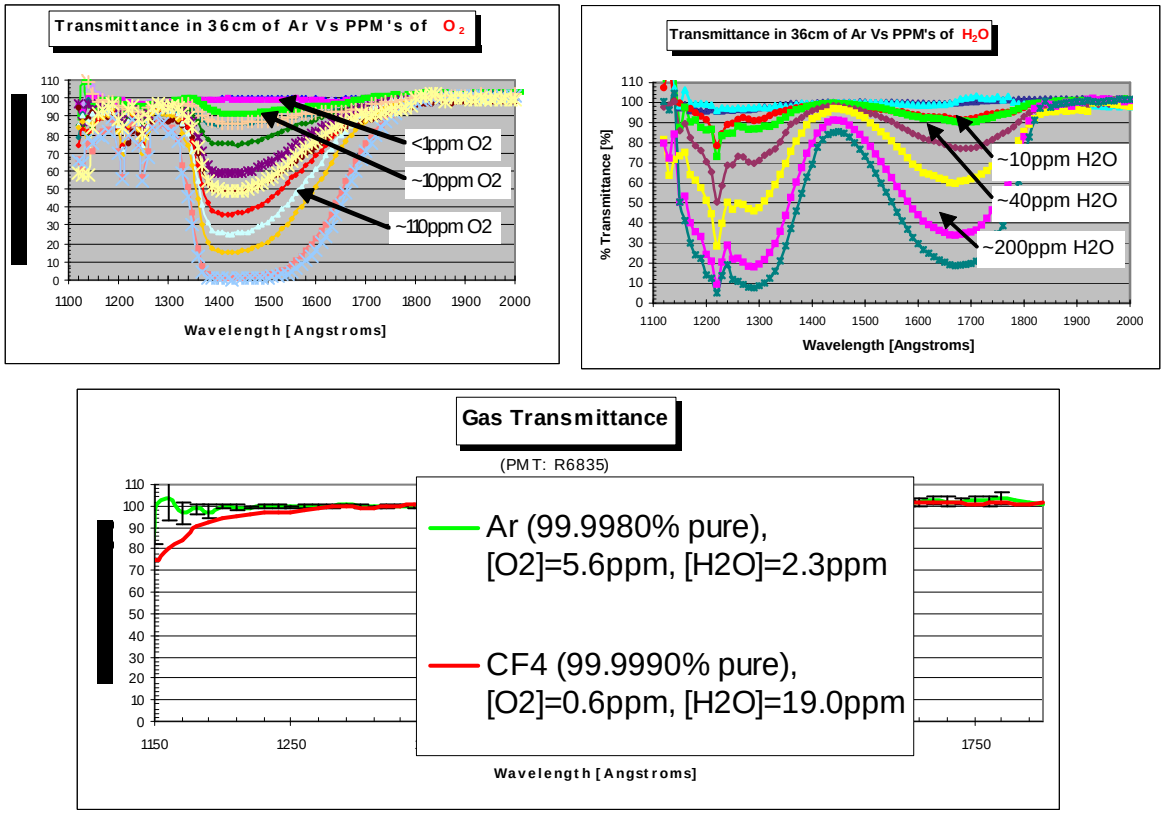

Figs. 39-41: VUV transmission measurements [9].

With proper gas flow and monitoring established, exterior work on the detector went forward. This involved several steps, including preamplifier installation, ground and noise studies, and developing a heating/cooling system for the vessel and the preamplifiers.

5.2 Preamplifier Installation

The circuit boards containing the pad readout electronics were installed, wired, and tested. Next, the preamplifier boards are installed onto the circuit boards and powered up (576 per side, 1152 on the detector total). To combat noise, a ground-sheathing scheme was employed, using wire braid and conducting

copper tape to interconnect all of the detector's external planes together. A foam and foil shield was installed over top of the preamplifiers and the foil was connected into the ground planes as well. Noise studies demonstrated a 100-fold decrease in noise after the plane was completed (200mV to 2mV).

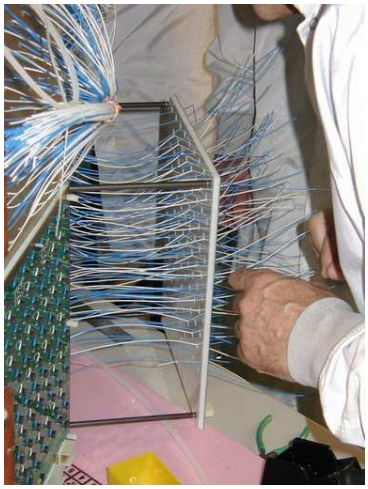

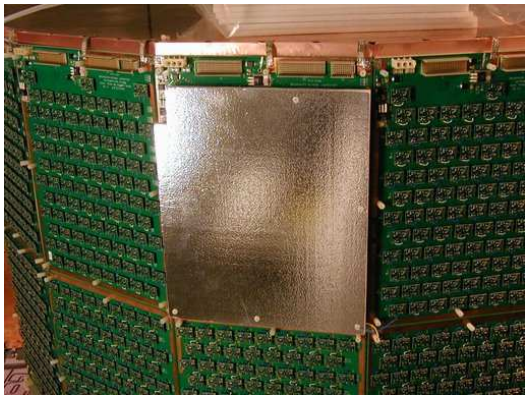

Figs. 42-44: Installing preamplifier circuit boards, one of the first preamplifier shields, grounding braids to improve noise characteristics.

5.3 Heating System

To increase the water outgassing rate from the internal surfaces of the detector, a heating system was employed to gently warm the external planes of the detector. This system utilized the same hardware as our evaporation box heating scheme. Temperature probes consisted of platinum RTDs, a Minco CT16A handled measurement and feedback control, and the heaters were large area Kapton foil heaters. The system had modest success at increasing the internal gas temperature, mostly due to the fact that the copper layer on the outside of the detector was thin compared to the volume of FR4 honeycomb and gas inside the detector. To experiment further, two other methods of heating were employed, heating wire was applied directly to the gas intake line (made of stainless braid), and infrared heating lamps were set up to irradiate the outer surfaces of the detector vessel. When vigorous heating was applied through all three systems, a rise in the gas water content was visible (from 12-15ppm up to ~20ppm). The main factor in water content seemed to be ambient temperature of the lab, however. During the day, when the LINAC was running in the next room, ambient temperature raised on the order of $10^{\circ}C$, and the water monitoring demonstrated a clear response between daytime (LINAC operating) and nighttime (LINAC off) temperatures. The Kapton™-foil heating system has been retained for use in the PHENIX experiment hall, it uses a combination of RTDs and

thermocouples to measure temperatures on the vessel surface and around the preamplifier cards to indicate overheating and maintain the feedback systems.

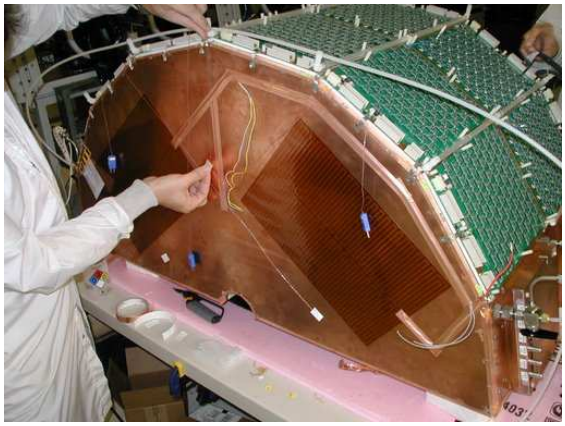

Fig. 45: Installing external heating system components.

5.4 Cooling System

In addition to heating, a cooling system was deemed necessary to maintain preamplifier performance. The preamplifiers generate a lot of heat, and they sit under a foam and foil shield, so the air gaps for convection are greatly reduced. First principle calculations were undertaken to ascertain the amount of heat being generated by the preamplifiers.

$$P = V \times I$$
$$P_1 = +5V \times 1.8A = 9W$$
$$P_2 = -5V \times 1.2A = 6W$$
$$P_{tot} = 15W$$

Then, further calculations and studies were undertaken to develop a forced air-cooling system to keep the preamplifiers reliable in operation. First, an upper limit of air requirement for one preamplifier board was determined:

$$15W = 15\frac{J}{s}$$

Air $\approx$ ideal diatomic gas, $C_P = \frac{7}{2}R$

Allow a $20^{\circ}C$ rise in temperature.

$$Q = nC_P\Delta T$$

$$15\frac{J}{s} = n\left(\frac{7}{2}\right)(8.315)20^{\circ}C$$

$$n = 0.026\frac{moles}{s}$$

$$V = \frac{0.026\frac{moles}{s}}{0.040\frac{moles}{L}} = 0.64\frac{L}{s} \approx 38\frac{L}{m} \approx 1.4cfm \approx 80cfh$$

Next, it was decided that a few measurements were needed to confirm the air requirements. One preamplifier board was fitted with a $\frac{3}{8}$" tube, given 2.5" of H_2O for head pressure, and bored with 5 small, uniform holes to provide $\approx$ equal flow @ reasonable pressure. Preamplifier temperature was then plotted as a function of flow and a $50cfh$ flow was decided as adequate, since there are 6 boards per side, this means $300cfh$ per side or $5cfm$ per side. Next, a manifold needed to be developed based on our observations so far. We wanted to deliver $5cfm$ through each branch of the manifold, with a head pressure of 2.5" of H_2O.

Now, Poiseuille's equation was modified to determine the manifold branch radius to achieve our flow goals.

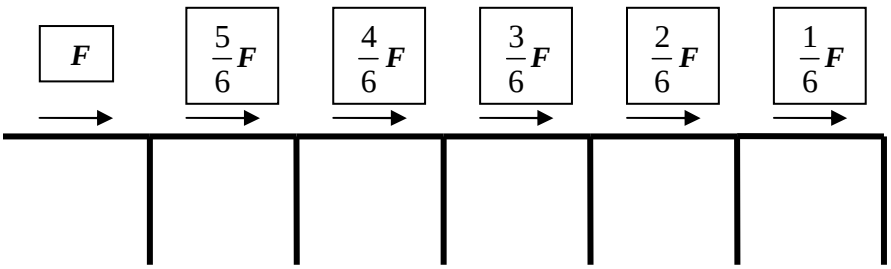

Fig. 46: Conceptual manifold layout.

Using Poiseuille's Law to determine manifold tube radius:

$P_{final} = 2.5"$ of H_2O

$\Delta P_i = F_i R$

$\Delta P_{total} = \sum_i \Delta P_i = \frac{15}{6} FR,$ where $R = \frac{8\eta L}{\pi r^4}$

$\eta = 1.8\times10^{-5} Pa\bullet s,\ L = 15",\ \Delta P_{total} = 0.2"$ of H_2O

Rearrange and solve for r:

$$r = \left(\frac{15F(8\eta L)}{6\pi\Delta P} \right)^{\frac{1}{4}} = 0.26"$$

$ID = 0.52",$ since flow is not perfectly laminar

increase ID to 0.75"

After completing this exercise the system was mocked up in prototype form, mimicking the pressure, flow, and physical requirements of a permanent installation, and the system performance was tested. The prototype system worked without a hitch and demonstrated excellent performance for the designed parameters. The system installed in the PHENIX experiment hall has been installed with no major changes with respect to the prototype design.


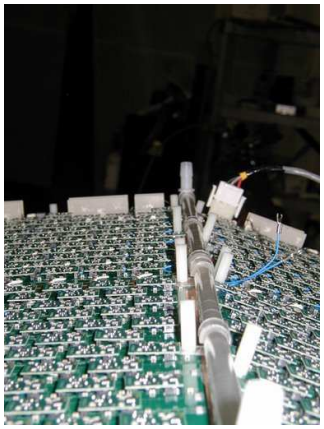

Figs. 47, 48: Prototype cooling system, and final placement in between preamplifiers.

5.5 Flash Lamp Tests

As a final test before preparing to transport the detector to BNL, where it would undergo high voltage conditioning (the HBD has completed activities in Run 7 at the time this thesis was written), a *Xe* flash lamp was used to test for photosensitivity on the GEM stack. A Perkin-Elmer flash lamp was wired to strobe through one of the vessel windows installed on the side of the detector (*LiF*). The mesh was powered with a *-100V* bias and the top GEM was coupled

with the oscilloscope to search for induced signal from the flash. Once each module had been tested, the detector was declared ready to move, and the system was prepared to transport and installation in the PHENIX experiment hall.

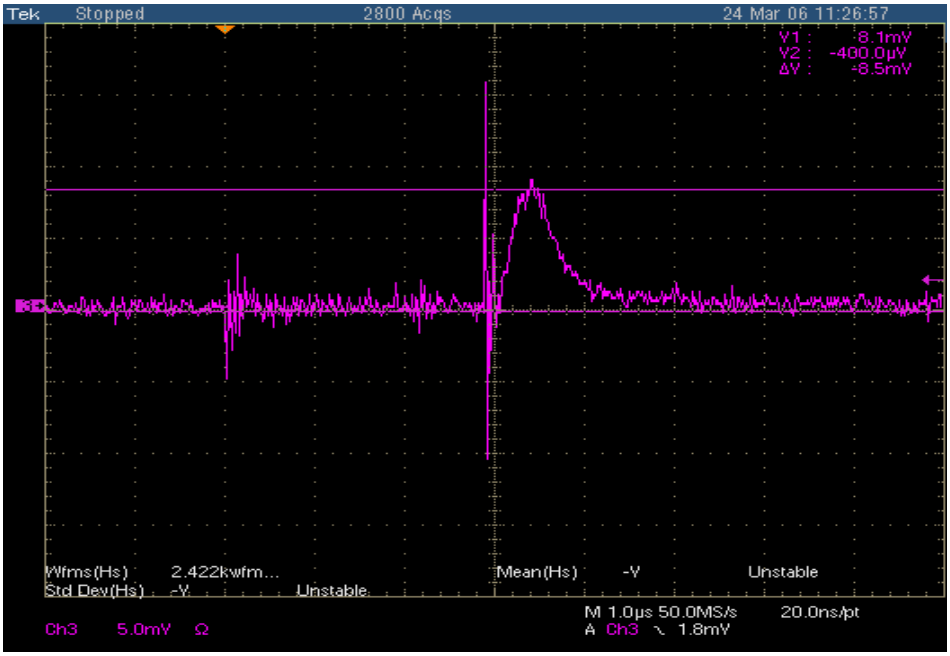

Fig. 49: Flash lamp testing (2 RF pulses, followed by a PE peak)

5.5.1 Commissioning Discussion:

Noise: The noise studies were just a quick and routine check to ensure that all 1152 channels were behaving in a manner that would interface neatly with the PHENIX FEM/DAQ and would have clean signals for determining e^+e^- pairs versus the ionizing particles created during collisions. Various ground schemes were played with until the noise levels were deemed satisfactory (*~2mV*).

Water/Oxygen/Heating: Considerable time was devoted to trying to increase the temperature of the vessel interior, beyond what the ambient was capable of. Most efforts towards heating had little effect, but the external Minco system was retained for final installation. Water and oxygen levels were observed to drop over time, and once stability was reached in accordance with the performance capabilities of our gas system, the HBD was declared ready for survey, transport, and installation.

Cooling: The cooling system performed as anticipated and has been implemented into the final installation at the experiment hall. Although we used bottled gas to mimic the flow of forced air, the final design of the system included Micronel® radial blowers that meet the pressure, volume, and flow characteristics parameterized by the prototype, gas bottle system. So far, the system has proven to be fully adequate for the purpose.

Lamp Test: The lamp test provided a final diagnostic to make sure the GEM stacks were still at least operational. The fact that consistent signals could be seen on GEMs with a pulse of light introduced into the interior validated the HBD integrity for transport and installation (since the glovebox is the only environment where the vessel can be opened, it was completely necessary to make sure the detector was operational prior to shipping).

6.0 Conclusions

This thesis outlined some of the manufacturing techniques responsible for the construction and implementation for a Hadron Blind Detector (HBD) that is being used to enhance the functionality of the PHENIX collaboration at the Relativistic Heavy Ion Collider (RHIC) located at Brookhaven National Laboratory. The main physics goal of the HBD is to improve the signal to background ratio of the PHENIX data through the process of e^+e^- veto. The design constraints on the HBD led to the development of many novel concepts, including the use of a blob imaging windowless Cherenkov detection scheme via GEMs. To ensure hadron blindness while maintaining e^+e^- sensitivity, a top-level mesh is employed with a reverse bias. The criteria set forth for the detector drove the development of new construction methods for large area *CsI* deposition techniques and the development of on-site high purity environments for construction, testing, and experimentation. The facilities and methods developed over the course of the HBD construction will be developed further for the next generation of GEM detectors (for repair/maintenance of the HBD) and can be adapted to a wide range of uses in future detector development.

Appendix

Section 1: Pre-Prototype Images

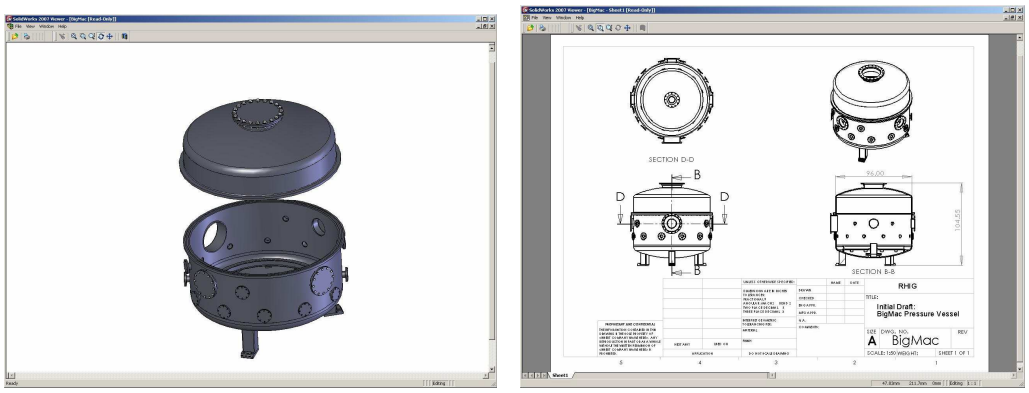

Figs. 50, 51: Modeling the Big Mac, preparing for conversion.

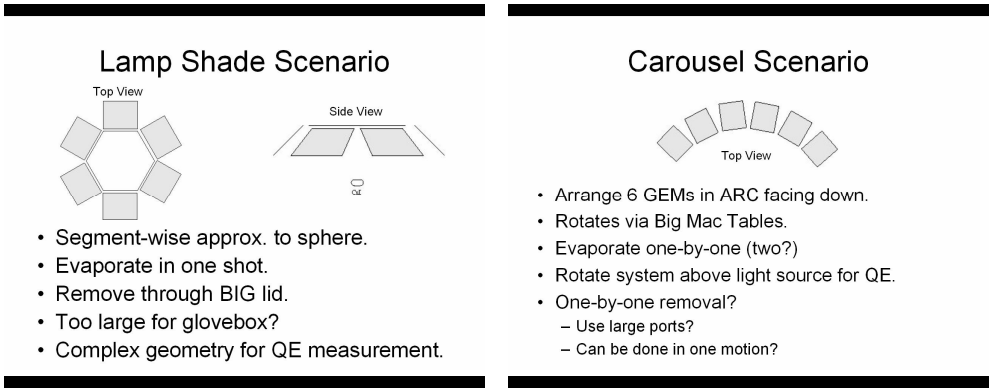

Figs. 52, 53: Early geometries for *CsI* evaporation inside Big Mac.

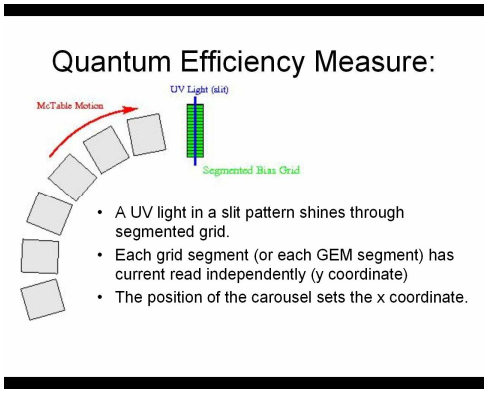

Fig. 54: Early QE concept for Big Mac.

Section 2: Prototype Construction

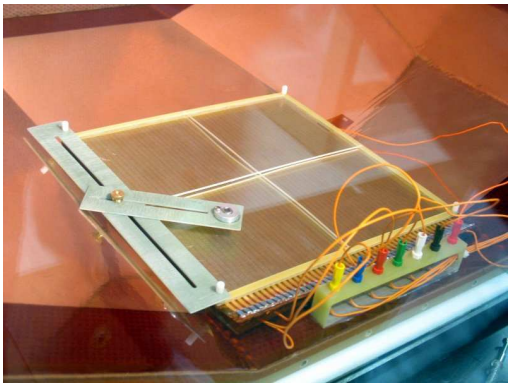

Figs. 55, 56: Single GEM stack in the prototype, prototype vessel in the old glove box.

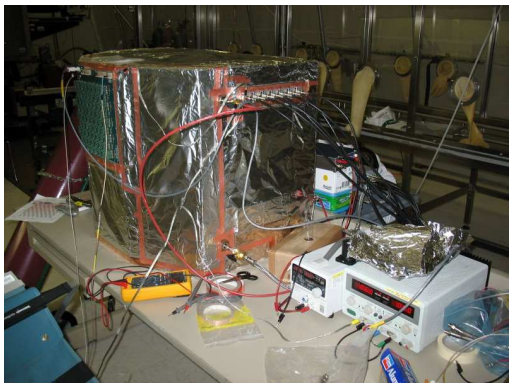

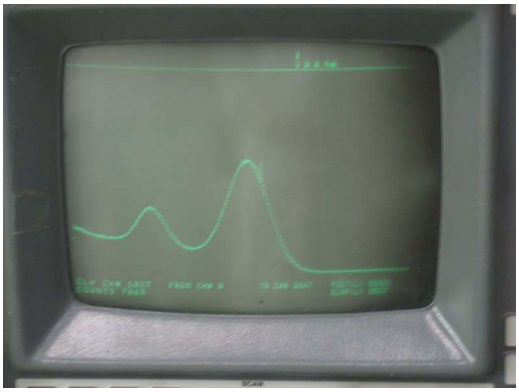

Figs. 57, 58: Completed prototype HBD undergoing testing, the first Fe^{55} peak on the prototype system.

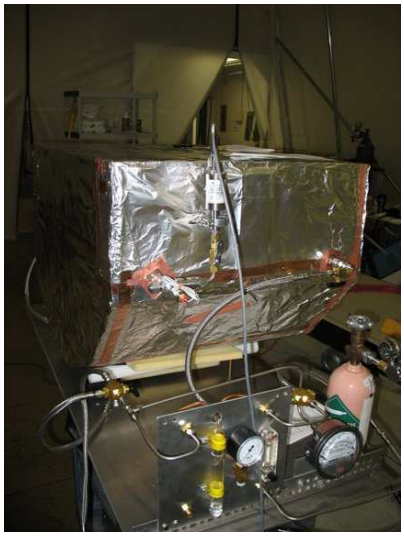

Fig. 59: Prototype HBD, under transport gas flow, awaiting shipment to BNL for Run 06.

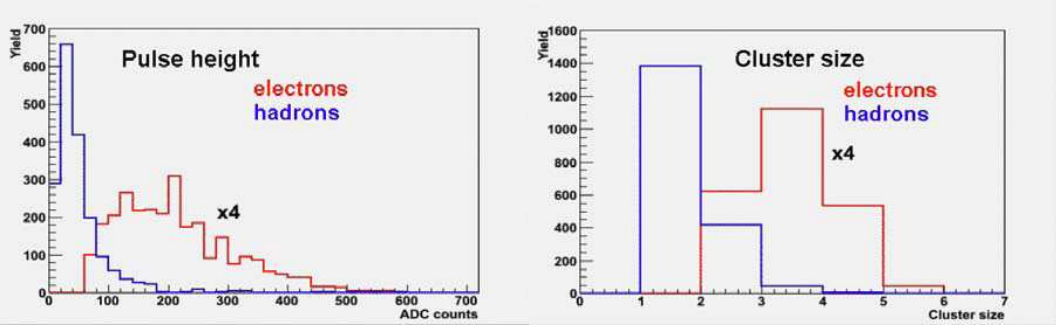

Fig. 60: Pulse height distribution (a) and cluster size distribution (b) for identified electrons and hadrons with the HBD prototype operated in reverse bias mode in PHENIX during the RHIC run 06 [14].

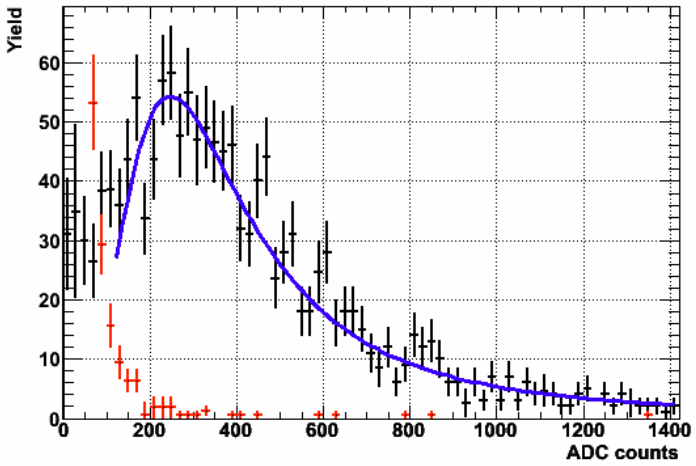

Fig. 61: Pulse height distribution for minimum ionizing particles obtained with the full scale HBD prototype operating in the PHENIX experiment during RHIC run 06. The forward bias distribution (black) is well fit with a Landau distribution, while the reverse bias distribution (red) shows the expected strong suppression of the direct ionization signal [14].

Section 3: Final Production Images

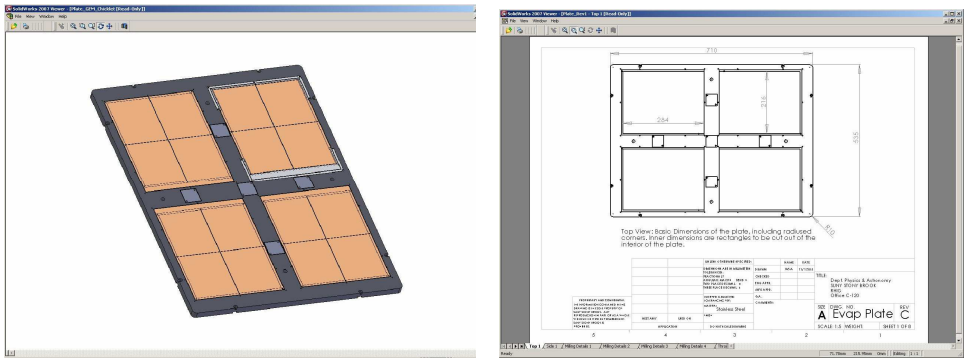

Figs. 62, 63: Evaporation frame design solid model and blueprints.

Fig. 64: Installing GEMs in the gain test station.

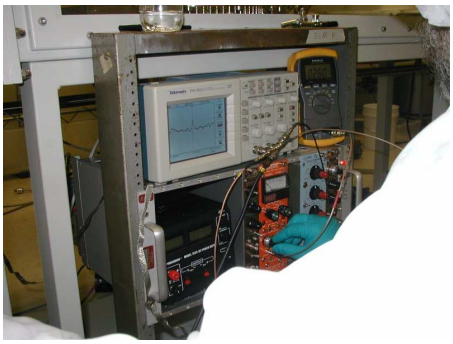

Figs. 65, 66: Running tests within the gain test station, building a tested GEM stack in the HBD.


Figs. 67, 68: Repairing GEM leads on the laminar flow table, all hands at work building HBD West.


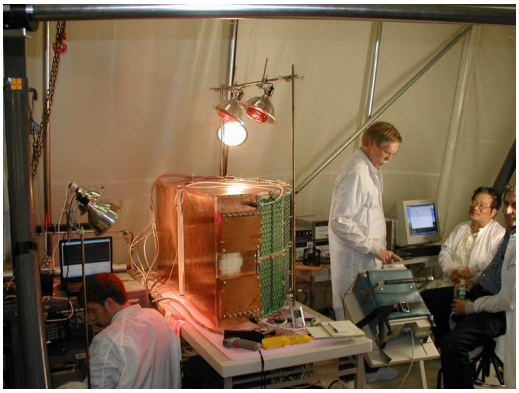

Figs. 69, 70: Voltage testing the preamplifier power components, running a battery of commissioning tests.

Section 4: Final Production Data

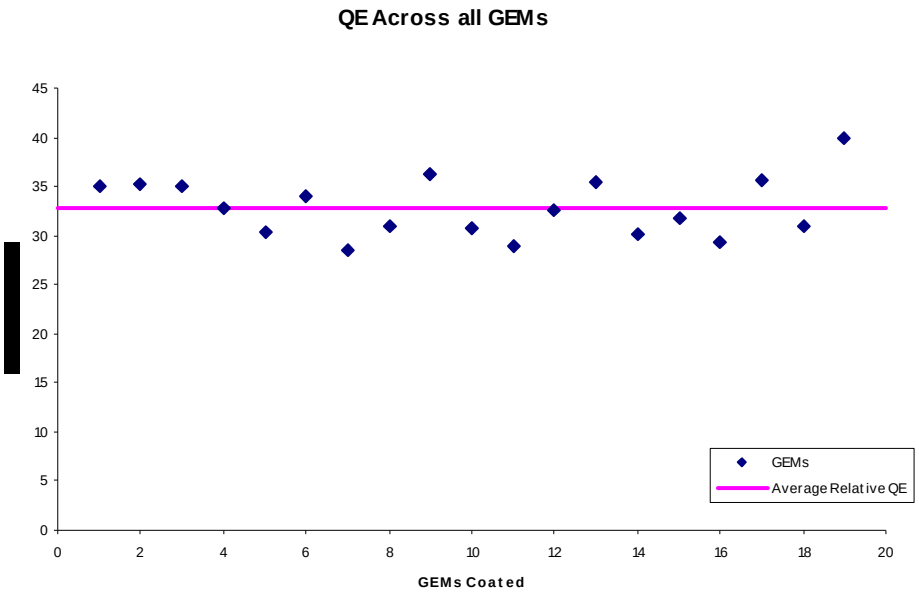

Fig. 71: GEM QE plot for average QE across all evaporations

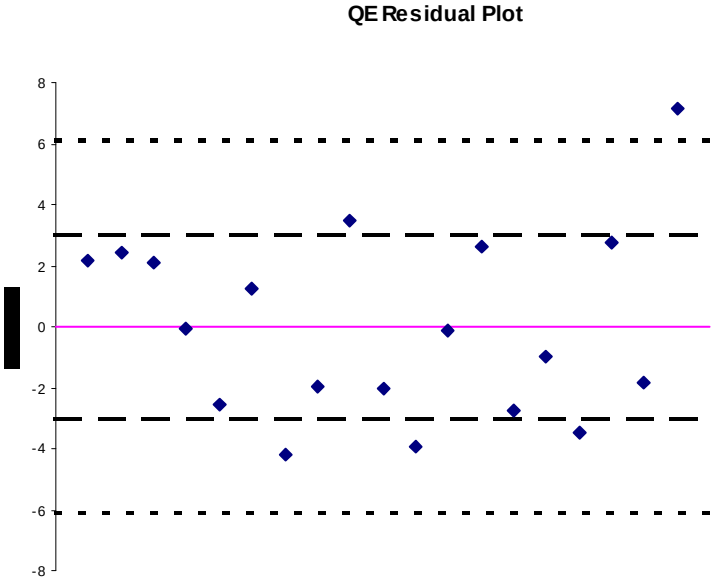

Fig. 72: Residual plot for QE evaporations.

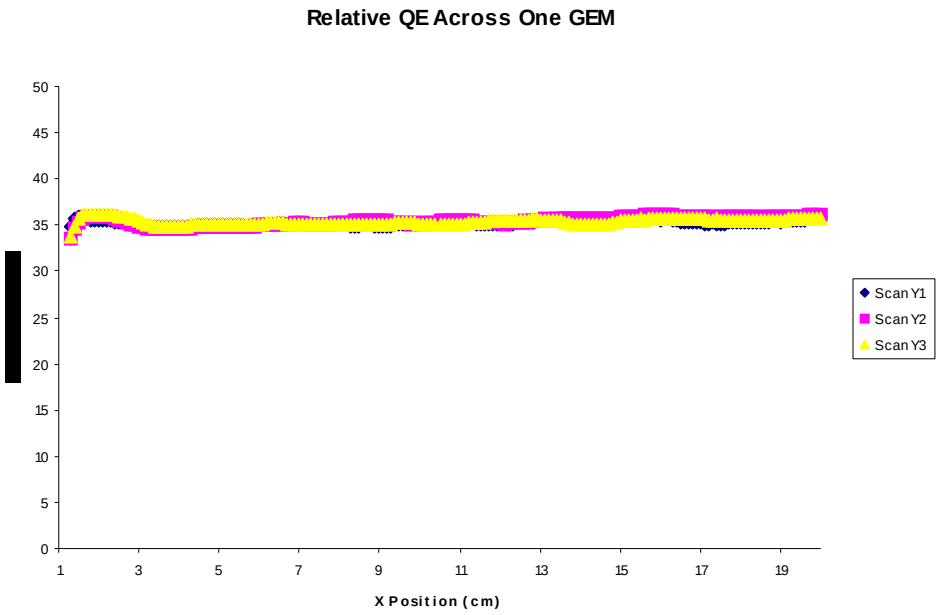

Fig. 73: Example QE scans across a single GEM (Three y-locations).

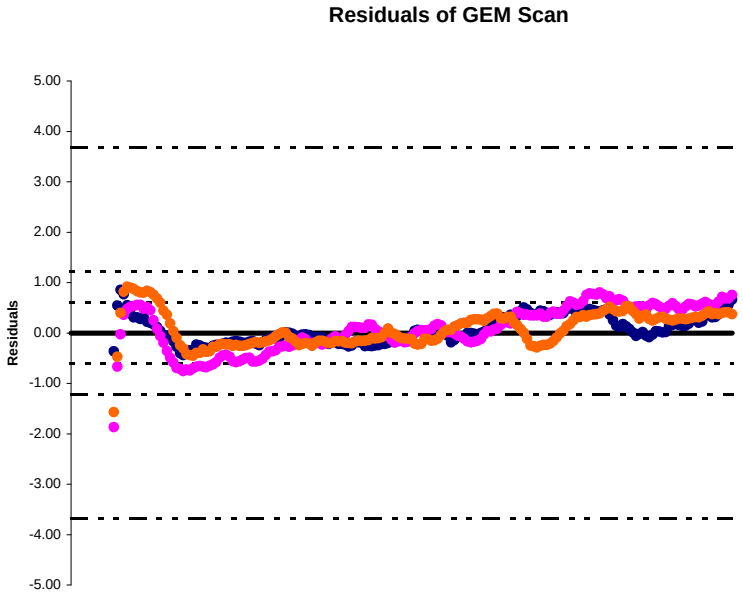

Fig. 74: Residuals for single GEM scan.

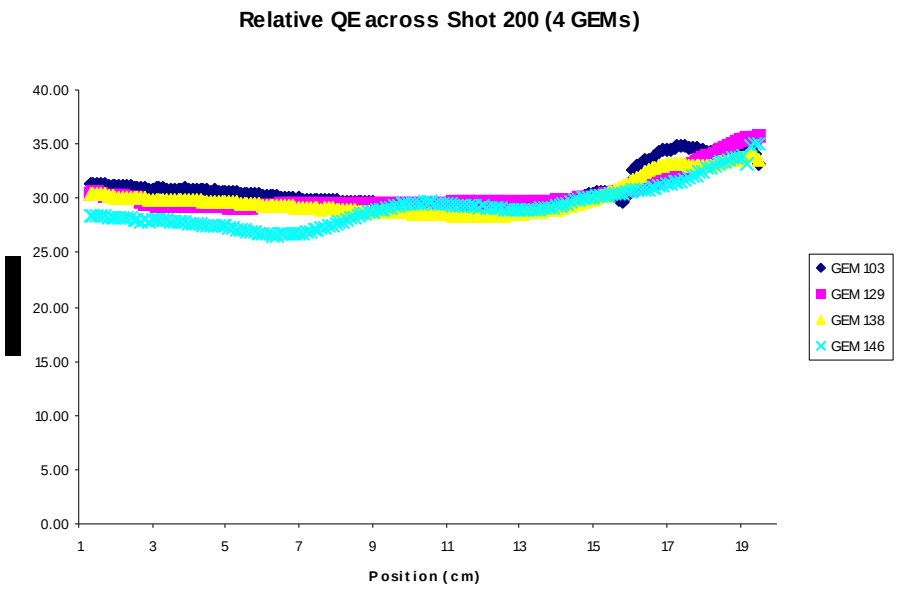

Fig. 75: Relative QE (Y-scans averaged) across the 4 GEMs of one shot.

References

[1] S. Adler, et al., ***Measurement of Direct Photon Production in p+p Collisions at*** $\sqrt{S_{NN}} = 200GeV$ **,** Phys. Rev. Lett. **98,** 012002 (2007).

[2] B. Azmoun, ***A Hadron Blind Detector for the PHENIX Experiment at RHIC***, CARRI Talk. October 13, 2004.

[3] B.Azmoun et.al., ***Conceptual Design Report on a HBD Upgrade for the PHENIX Detector***, March (2005).

[4] B. Azmoun, ***A Study of the Prime Components of the HBD/TPC as Part of an Upgrade to PHENIX***; Master's Thesis: SUNY Stony Brook (2004).

[5] A. Drees, et al., ***PHENIX R&D Proposal***, PHENIX Collaboration, (2002).

[6] Z. Frankel et.al., ***A Hadron Blind Detector for the PHENIX Experiment at RHIC***, Nucl. Inst. Meth. A546 (2005) 466-480.

[7] J. Kamin, ***Hadron Blind Detector: Detector Talk***, PHENIX Focus Talk, January 23, 2007.

[8] A. Kozolov et.al., ***Development of a Triple GEM UV Photon Detector Operated in Pure*** CF_4 ***for the PHENIX Experiment***, Nucl. Inst. Meth. A523 (2004) 345.

[9] S. Milov, ***Hadron Blind Detector for the PHENIX Experiment at RHIC***, Conference Proceedings, CIPANP 2006, August 23, 2006.

[10] F. Ronchetti, ***Deuteron photomeasurement data analysis***, N* Conference (1998).

[11} F. Sauli, ***Novel Cherenkov photon detectors***, Nucl. Inst. And Meth. A553 (2005) 18-24.

[12] F. Sauli, ***Development and applications of gas electron multiplier detectors***, Nucl. Inst. And Meth. A505 (2003) 195-198.

[13] I.Tserruya et.al., ***A Hadron Blind Detector for the PHENIX Experiment at RHIC***, Conference Record Proceedings, IEEE NSS (2004).

[14] C. Woody, et al. Prototype Tests and Construction of the Hadron Blind Detector for the PHENIX Experiment, Conference Record Proceedings, IEEE NSS (2006).